The Influence of Autumnal Eurasian Snow Cover on Climate and Its Link with Arctic Sea Ice Cover

Guillaume Gastineau, Javier García-Serrano, Claude Frankignoul

1

The influence of autumnal Eurasian snow cover

on climate and its link with Arctic sea ice cover

4

5

Guillaume Gastineau*[1], Javier García-Serrano[2]

and Claude Frankignoul[1]

[1]Sorbonne Universités, UPMC/CNRS/IRD/MNHN, LOCEAN/IPSL, Paris,

France

[2]Barcelona Supercomputing Center (BSC), Barcelona, Spain

14

15

May 15th, 2017

17

Corresponding author address: Dr Guillaume Gastineau, Sorbonne Universités,

UPMC/CNRS/IRD/MNHN, LOCEAN/IPSL, 4 place Jussieu, 75005 Paris, France.

E-mail: guillaume.gastineau@upmc.fr

21

22   Abstract:

23

24   The relationship between Eurasian snow cover extent (SCE) and Northern

25   Hemisphere atmospheric circulation is studied in reanalysis during 1979-2014 and in

26   CMIP5 preindustrial control runs. In observations, dipolar SCE anomalies in November,

27   with negative anomalies over eastern Europe and positive anomalies over eastern

28   Siberia, are followed by a negative phase of the Arctic Oscillation (AO) one and two

29   months later. In models, this effect is largely underestimated, but four models simulate

30   such relationship. In observations and these models, the SCE influence is primarily due

31   to the eastern Siberian pole, which is itself driven by the Scandinavian pattern (SCA),

32   with a large anticyclonic anomaly over the Urals. The SCA pattern is also responsible for

33   a link between Eurasian SCE anomalies and sea ice concentration (SIC) anomalies in the

34   Barents-Kara Sea.

35   Increasing SCE over Siberia leads to a local cooling of the lower troposphere, and

36   is associated with warm conditions over the eastern Arctic. This leads to a polar vortex

37   weakening in December and January, which has an AO-like signature. In observations,

38   the association between November SCE and the winter AO is amplified by the SIC

39   anomalies in the Barents-Kara Sea, where large diabatic heating of the lower

40   troposphere occurs, but SCE is the main driver of the AO. Conversely, the sea ice

41   anomalies have little influence in most models, which is consistent with the less

42   frequent SCA, the colder mean state, and the underestimation of troposphere-

43   stratosphere coupling in these models.

44

1. Introduction

The role of Arctic conditions in the mid-latitude winter climate is under debate, especially for the North Atlantic sector (Overland et al. 2015). In this region, the atmosphere has a dominant short-timescale chaotic intrinsic variability and is mainly unpredictable. However, several studies suggest that the variability of Arctic sea ice extent (Yamamoto et al. 2006; Francis et al. 2009; Honda et al 2009; Wu and Zhang 2010; Frankignoul et al. 2014; Garcia-Serrano et al. 2015, Koenigk et al. 2016, King et al. 2016) and Eurasian snow cover extent (SCE, e.g. Cohen and Entekhabi 1999, Cohen et al. 2007, Cohen and Jones 2011) have some influence onto the atmosphere during winter. Such influence may account for an improvement in skill of long-range prediction due to continental snow (Jeong et al., 2013, Orsolini et al., 2013) and sea ice (Scaife et al. 2014) initialization and improved continental snow cover physics (Riddle et al. 2013) in current forecast systems.

Continental snow cover affects the atmosphere via changes in surface albedo (Cohen 1994). A larger snow cover increases the surface albedo and reflects shortwave radiation away from the surface (Gong et al. 2004, Jeong et al., 2013). A snowpack also insulates the atmosphere from the soil surface. In winter at high latitude, these two effects explain that snow enhances the diabatic cooling at the surface and in the atmospheric boundary layer (Fletcher et al. 2007; Dutra et al. 2011), which locally increases the sea level pressure (SLP). A larger SCE over Eurasia has been reported to intensify and expand the Siberian high (Jeong et al., 2011; Orsolini et al., 2013). This modifies the land/sea contrast and the stationary wave pattern, and may lead to enhanced upward planetary wave propagation, thus weakening and warming the polar vortex in the stratosphere (Saito et al., 2001, Cohen et al. 2007, Orsolini et al., 2016). A weak polar vortex can persist for several weeks and influence the underlying

70   troposphere by downward propagation of circulation anomalies. The influence of the

71   Eurasian snow cover has received most attention in autumn, as it shows a statistically

72   significant relation with the following winter Arctic Oscillation (AO) and North Atlantic

73   Oscillation (NAO), from December to March (Cohen et al., 2007; Déry and Brown, 2007;

74   Allen and Zender, 2010; Cohen et al., 2012).

75   Sea ice concentration (SIC) changes may also influence the atmosphere. The most

76   reported influence concerns SIC in the Barents-Kara Sea, where SIC in autumn has a

77   statistically significant influence on the following winter NAO (Petoukov and Semenov,

78   2010; Kim et al., 2014; Garcia-Serrano et al., 2015; King et al., 2016). Sea ice insulates

79   the ocean from the atmosphere, so that a sea ice loss increases the heat flux from the

80   ocean to the atmosphere. The resulting diabatic heating is large, but localized near the

81   sea ice edge (e.g. Magnusdottir et al. 2004; Deser et al. 2004, 2007). This leads to

82   changes in the tropospheric eddies and the planetary wave pattern, which may alter the

83   polar vortex (e.g. Nakamura et al. 2015, 2016). The modified polar vortex may then

84   influence the troposphere by downward propagation in the following weeks or months,

85   with important impacts during periods of polar vortex breakdown, such as in February

86   (Jaiser et al. 2016).

87   The influence of SIC thus shares a large similarity with that of the Eurasia SCE

88   during fall (October and November), as both may involve a stratospheric pathway.

89   Furthermore, continental SCE and Arctic SIC are linked, as a reduced Arctic sea-ice

90   extent leads to a moistening of the atmospheric boundary layer, which increases the

91   moisture flux into eastern Siberia, increasing snowfall, as suggested by Cohen et al.

92   (2014a) and found by Wegmann et al. (2015) using a Lagrangian analysis. The sea ice

93   and snow cover are also connected by the influence of Ural Blocking, which has been

94   reported to cause warm Arctic–cold Eurasia anomalies in winter (Luo et al., 2016). The

4

95 two surface influences are, therefore, connected, and their interaction might amplify the

96 atmospheric response found by separately considering snow cover and sea ice (Cohen et

97 al. 2014a). However, only a few studies have investigated the links between the SCE and

98 sea ice. Moreover, the relative effect on the atmosphere of the Arctic sea ice and

99 Eurasian snow cover is largely unknown. In addition, the influence of tropical SST

100 variability needs to be clarified, as the tropical teleconnections may both influence the

101 snow cover over Eurasia and modify the atmospheric circulation (Fasullo, 2004), leading

102 to a possible confusion between cause and effect.

103   As the observational record is mostly limited to the recent decades, climate

104 models can be used to investigate the impact of SIC and SCE variability with a much

105 larger sampling, even if the stratospheric polar vortex is too stable in models, which may

106 inhibit the troposphere-stratosphere coupling (Furtado et al., 2015). The aim of this

107 study is to investigate the influence of autumnal Eurasian snow cover variability in

108 observations and climate models, and the links with that of the sea ice cover. We find

109 that snow cover anomalies in November have a dominant influence on the atmospheric

110 circulation in observations and several models. The SCE anomalies are found to be

111 associated with SIC anomalies over the Barents-Kara Sea, as both are modulated by the

112 Scandinavian pattern, which is the dominant mode of atmospheric variability in

113 November.

114   The next section describes the methodology. The analysis of the snow cover and

115 its links with the atmosphere is discussed in Section 3. The processes linking the snow

116 cover to the atmosphere are investigated in Section 4. Finally, conclusions and a

117 discussion are provided in last section.

118

119

2. Data and methods

a. Observations

Monthly sea ice cover is downloaded from the NOAA/National Snow and Ice Data Center (Comiso, 2012). Weekly Northern Hemisphere continental snow cover is retrieved from the NOAA/Rutgers University Global Snow Laboratory, and aggregated into monthly data. Both products are based on passive microwave measurements (SSM/I) and extend from 1979 to 2014. The sea-level pressure (SLP), geopotential height, air temperature, and heat flux (accumulated from 24h forecasts) are from the ERA-Interim reanalysis (Dee et al., 2011).

A quadratic trend is removed from all variable before the analysis to remove the effect of the global warming. This also removes the multi-decadal variability and lower frequencies, and the large Arctic sea ice decrease from 2005 onward (e.g. Close et al. 2015).

b. Models

Monthly SLP, snow cover, geopotential, SIC, SST and heat fluxes anomalies are downloaded from the CMIP5 archive for 12 coupled ocean atmosphere models (Table 1) using the preindustrial multi-centennial control simulations with constant external forcing. All model fields are interpolated onto a common 2.5°x2.5° horizontal grid. A quadratic trend was removed from all outputs to remove the possible influence of model drift.

c. Maximum covariance analysis

Maximum covariance analysis (MCA) is used to estimate the main modes of area-weighted covariability between the atmosphere and the underlying snow cover. We use

6

145 snow cover anomalies over northern Eurasia (40°N-65°N;0°E-180°E). The SLP

146 anomalies in the Northern Hemisphere (20°N-90°N) are chosen to represent the

147 tropospheric circulation. The MCA decomposes the covariance matrix of the two fields

148 using singular value decomposition (Bretherton et al., 1992). Each mode of covariability

149 is characterized by two times series and associated spatial patterns. Here, the MCA time

150 series are standardized (divided by their standard deviation). The spatial patterns are

151 illustrated by the homogeneous covariance map for the field that leads (regression on

152 the same field time series) and the heterogeneous covariance map for the field that lags

153 (regression on the MCA time series of the other field), which preserves orthogonality

154 (Czaja and Frankignoul, 2002). The MCA modes are characterized by their normalized

155 squared covariance (NSC, i. e. the squared singular value divided by the variance of both

156 fields), the correlation (R) between the MCA time series, and the squared covariance

157 fraction (SCF, i. e. the ratio of covariance explained). In order to evaluate the robustness

158 of the MCA modes, we repeated the MCAs using 100 random permutations of three-

159 years blocks for the SLP field. The number of NSC and R that exceed the observed values

160 gives the levels of significance for NSC and R.

161   The mode of covariability between the snow cover and the atmosphere are

162 expected to reflect the influence of atmospheric perturbations on the SCE when the two

163 fields are in phase or, because of snow cover persistence, when the atmosphere leads.

164 When the snow cover leads the atmosphere by one month or more, a significant MCA

165 mode could indicate an influence of the snow cover (or concomitant boundary forcing)

166 on the atmosphere, as the extratropical atmosphere has an intrinsic persistence of at

167 most 10 days (Vautard, 1990). However, the El Niño Southern Oscillation (ENSO) has

168 persistent remote teleconnections that may give rise to persistent MCA modes not solely

169 linked to local boundary forcing. Hence, we (largely) remove these teleconnections from

170 both snow and atmospheric data by multivariate regression when (and only when) the

171 snow cover field leads the atmosphere, assuming that they lag the tropical Pacific SST by

172 two months in the atmosphere, while they vary with lag for the snow in order to get

173 unbiased estimates (see Frankignoul et al., 2011). The tropical SST variability is

174 represented by the first three empirical orthogonal functions (EOFs) of the monthly

175 tropical Indo-Pacific SST. The regressions are performed separately for each season, to

176 account for the seasonal changes of the ENSO teleconnection, and separately for positive

177 and negative values of the Principal Components (PCs), to account for the asymmetry

178 (see supplemental material text for details). We verified that similar MCA results are

179 obtained by assuming a one-month lag for the ENSO teleconnections, or even without

180 removing the ENSO signal (see Table S1).

181

182   *d. Rotated empirical orthogonal function*

183   The main patterns of Northern Hemisphere (20°N - 90°N) SLP variability are

184 given by rotated empirical orthogonal function (REOFs) analysis, using the first 15 EOFs

185 in the rotation, which accounts for 95% of the variance. To preserve orthogonality of the

186 PCs, we scaled the EOFs by the square root of its eigenvalue before performing the

187 varimax rotation (Kaiser 1958). The rotated PCs are standardized, and the REOF

188 patterns are given by regression on these time series.

189

190   *e. Regression analysis*

191   We used both univariate and multivariate least squares regression. We remove

192 the tropical teleconnections from all data before the regression analysis, following the

193 same methodology as the MCA (see section 2.c). The level of statistical significance is

194 tested with 100 permutations of the atmospheric fields in 3-yr blocks to take serial

195 autocorrelation into account. The number of permuted regression slopes that exceeds

196 the observed value provides the p-value.

197

3. The links between Eurasian snow cover and the atmosphere

199   *a. Detection of the snow cover influence*

200   The normalized squared covariance (NSC) of the first MCA mode provides an

201 estimate of the dominant covariability between the SCE and SLP anomalies. It is shown

202 as a function of lag and season for the observations in Fig. 1. The largest NSC are mostly

203 obtained when the atmosphere is in phase with the SCE or leads it by one month

204 (negative lag), reflecting that the atmosphere controls the formation of snow cover

205 anomalies. The largest covariability occurs for SLP in March at lag 0 and for SLP in

206 February when it leads by one month. This is consistent with the occurrence of the

207 largest interannual snow anomalies in March, and the largest atmospheric variability in

208 February.

209   At positive lag, the snow cover leads the atmosphere, which may reflect the SCE

210 forcing of atmospheric anomalies. The most significant links are found between

211 November snow cover and SLP in December (lag 1) and January (lag 2), as well as

212 between February snow cover and SLP in March (lag 1), as the NSC and R are both

213 significant at the 5% level (Fig. 1). The covariability is weaker when October SCE leads

214 the atmosphere, whether by 1, 2 or 3 months (p-values are 10%, 28%, 40% for NSC and

215 13%, 38%, 20% for R). Our results thus contrast with the commonly argued impact of

216 October Eurasian snow cover on winter SLP (Saito and Cohen, 2003), as further

217 discussed in Appendix. A significant covariance (p-value<10%) is also found for SLP in

218 August and September, when the snow leads by one month.

9

219   The influence of November SCE onto the atmosphere in December and January is

220   the main focus of this paper, and it is discussed below. The late winter snow influence

221   found in March has been reported in several studies (Barnett et al., 1989; Saito and

222   Cohen, 2003; Zhang et al., 2004; Peings and Douville, 2010; Peings et al. 2011); it is not

223   investigated here, as the processes are different from the fall influence studied here.

224   Similarly, the covariability in late summer is not discussed here; it shows a reduction of

225   snow cover in south-western Norway preceding anticyclonic conditions over the North

226   Atlantic (not shown), and might be due to concomitant North Atlantic SST forcing

227   (Gastineau and Frankignoul, 2015).

228   The same analysis has been performed with the CMIP5 models, and a significant

229   covariability between SCE and SLP anomalies is found in several cases. The results are

230   summarized in Fig. 2, which shows the level of statistical significance of the NSC and R

231   for the first MCA mode (left panel). The similarity with the observational data is given

232   by the spatial pattern correlation of the homogeneous SCE and heterogeneous SLP

233   covariance maps between each model and the observation (right panel). When using

234   November SCE anomalies and December SLP (black symbols in Fig. 2), there are four

235   models out of 12 (CanESM2, MPI-ESM-LR, GISS-E-R and CESM1) suggesting an impact of

236   the November SCE anomalies that is reasonably similar to that observed (spatial

237   correlation between 0.2 and 0.9). These four models show a first MCA mode that is 10%

238   significant for NSC and R, except for MPI-ESM-LR, which is only 12% significant for R.

239   Among these four models, only CESM1 is a low-top model, while the others are high top

240   models with lid height above 45km (Seviour et al., 2016).

241   The SCE influence seems to be less persistent in models, as the first MCA mode

242   with November SCE is only significant at lag 2 (SLP in January) in CESM1 (red symbols

243   in Fig. 2), as opposed to observations (Fig. 1). When using October SCE and November

10

244   SLP (blue symbols in Fig. 2), there are only two models out of 12 suggesting an impact of

245   the October snow cover anomalies (CSIRO-Mk3-6 and CCSM4). When using October SCE

246   and December (January) SLP, only one model, FGOALS-g2 (IPSL-CM5A-LR), provides a

247   potential impact. We conclude that consistent with observations, more CMIP5 models

248   suggest an impact of November SCE than October SCE. Next, we will discuss the spatial

249   patterns corresponding to these modes of covariability.

250

251   *b. Spatial pattern of the November snow cover influence*

252   The covariance maps for November SCE and December SLP are shown in Fig. 3. In

253   observations, the first MCA mode shows dipolar snow cover anomalies (Fig. 3a, colors),

254   with a pole over eastern Europe and an opposite polarity over south-eastern Siberia,

255   Northern Mongolia, and Northern China. Both poles are located at the margin of the

256   snow-covered surface in November (see Fig. S1). This SCE dipole precedes SLP

257   anomalies (black contours) broadly projecting on a negative phase of the AO, with a

258   large signature over the North Atlantic. The covariance maps at lag 2 (Fig. 3b, November

259   SCE / January SLP) are almost identical, but the SLP anomalies are weaker, especially

260   over Western Europe. Note that the covariance maps at lag 3 (November SCE / February

261   SLP) are also similar, although the significance level for NSC and R are 1% and 27%,

262   respectively.

263   The MCA patterns in the four CMIP5 models (CanESM2, MPI-ESM-LR, GISS-E-R,

264   CESM1) identified previously are broadly similar to the observed ones (Fig. 3c-f), with a

265   positive snow cover anomaly in southern Siberia and a negative one over eastern

266   Europe preceding a negative AO-like pattern by one month. However, the amplitudes

267   are smaller than in observations (note the different color and contour interval in Fig. 3).

268   Futhermore, the snow cover anomalies are slightly shifted, as the November SCE

11

269   climatology shows less snow over Eurasia, especially over Europe (Fig. S1). In the

270   following we only consider this subset of four models, as illustrated by the averaged

271   covariance map (Fig. 3g).

272   To take into account the different sampling in models (≥ 500 yr) and

273   observations (36 yr), we performed similar MCA analysis on separate 36-yr segments

274   from each of the four model simulations. These 36-yr segments are selected using a shift

275   of 6 years between two consecutive ones, so that for instance a 1000-yr run results in

276   160 36-yr segments. The mean NSC and R for the first MCA mode in these segments are

277   larger than the ones computed from the entire run (compare Fig. 3h and values on top of

278   Fig. 3c-f), but still smaller than in observations, with the 95% percentile of their

279   distributions lower than the observed value. Therefore, it is very likely that the models

280   do underestimate the snow influence.

281

282   *c. Origin of the snow cover dipolar variability in November*

283   To determine the origin of the dipolar snow cover anomalies, November SLP and

284   2m air temperature anomalies are regressed onto the (standardized) MCA time series of

285   November SCE, referred to as MCA-snow (Fig. 4). For the CMIP5 models, we only

286   consider the four models (CanESM2, MPI-ESM, GISS-E2-R and CESM-BGC) that are

287   consistent with observations and show the multi-model average of the regression

288   patterns, while the number of models with a regression of the same sign documents

289   their robustness, and provides a measure of inter-model spread.

290   The SLP anomalies associated with the snow dipole in both observations (Fig. 4a)

291   and models (Fig. 4b) are characterized by a large anticyclonic anomaly over the Urals

292   and a depression over Europe. The SLP pattern shares some similarity with the Eurasian

293   pattern type 1 (Barnston and Livezey, 1987), the Scandinavian pattern (Bueh and

12

294 Nakamura 2007), the Russian pattern (Smoliak and Wallace, 2015) or the anomalies in

295 Ural Blocking conditions (Luo et al., 2016). A similar pattern was also reported to result

296 from the October SCE response (Cohen et al., 2014b). We will refer to this atmospheric

297 patterns as the Scandinavian pattern (SCA) in the following. Figure 4 illustrates that

298 warm (cold) air temperature anomalies are associated with negative (positive) SCE

299 anomalies, consistent with the warm (cold) advection by the anomalous atmospheric

300 circulation, as in the Greenland, Barents and Kara Seas that are affected by warm

301 advection from the Norwegian Sea.

302   In observations, a dipolar SCE pattern similar to that in Fig. 3a and a SCA-like SLP

303 pattern is also obtained as first MCA mode of simultaneous SLP and SCE anomalies in

304 November, with 42.1% of squared covariance fraction (SCF), as shown in (Fig. 5a), while

305 an AO influence onto the snow cover is only obtained as mode 3 (SCF = 11.6%). This is

306 consistent with the first REOF of November SLP, which corresponds to the SCA (Fig. 6a).

307 In December, however, the simultaneous covariability between SLP and SCE is

308 dominated by the AO (SCF=55.1%, Fig. 5b), which decreases the advection from the

309 relatively warm ocean toward the cooler Eurasian Continent. It also shifts southward

310 the precipitation associated with the Atlantic stormtrack (Hurrell, 1995), which

311 increases the SCE over Europe. We also see negative SCE anomalies east of the Caspian

312 Sea associated with warm advection from the Mediterranean region.

313   On the other hand, the MCA suggests that, in most of the four models, the AO

314 already has the largest impact on snow cover in November (Fig. 5c), with a much larger

315 impact downstream of Europe, as shown by the positive anomalies over Eastern Siberia.

316 Only CESM1 simulates the SCA pattern and its dipolar snow cover signature as first MCA

317 mode (not shown). In fact, the first REOF of November SLP is also A0-like in all models

318 (Fig. 6b). To establish its robustness, we have used as above distinct 36-yr chunks from

13

319   each control simulation, to reproduce the observed sampling. The SCA and AO are

320   identified using the largest spatial pattern correlation with the observed SCA (November

321   REOF1) and AO (November REOF3), respectively. The AO variance fraction is

322   systematically larger than observed (Fig. 6c, yellow), while the SCA one is smaller (Fig.

323   6c, red). This is consistent with the larger (smaller) role of the SCA (AO) in the

324   observation, when compared to model simulations, and it can be explained by either

325   natural atmospheric variability or model biases. Indeed, CMIP5 models use relatively

326   coarse horizontal resolutions, and are known to underestimate winter blocking episodes

327   (Dawson et al, 2012), leading to an overestimation of the NAO regimes (Cattiaux et al.,

328   2013).

329

330   **4. Processes of the November snow cover influence**

331   *a. Role of Siberian snow cover*

332   The relative importance of the two poles of the November SCE dipole can be

333   analyzed using two indices: the mean SCE anomalies over eastern Europe (20°E-58°E,

334   48°N-60°N) and over eastern Siberia (70°E-140°E, 43°N-56°N). A bivariate regression of

335   SLP anomalies in December on these two indices shows significant SLP anomalies in the

336   observations (Figs. 7a and 7b), with negative SLP anomalies off Western Europe and

337   positive anomalies over the polar cap. However, the eastern Siberia pole has the largest

338   and most significant influence on SLP, and its impact is more AO-like. In the four models

339   (Figs. 7c and 7d), Siberian SCE anomalies also have a larger, AO-like influence on SLP,

340   while European SCE is linked to a weak SLP dipole between Greenland and Scandinavia.

341   Therefore, the most robust signal seems to be linked to the Siberian SCE influence,

342   which is consistent with the reported influence of October snow cover (Saito and Cohen,

343   2003).

344

345   *b. Associated surface changes*

346   The influence of surface conditions is evaluated using SCE and SIC regressions

347 onto MCA-snow in Fig. 8. The SCE anomalies in November (Fig. 8c,d) are preceded in

348 October (Fig. 8a,b) and followed in December (Fig. 8e, f) by similar, but smaller,

349 anomalies over eastern Siberia, which is consistent with the snow cover persistence

350 over that region (Déry and Brown, 2007), and reflected in the large correlation (around

351 0.5) between October and November SCE (see Fig. S1). European SCE anomalies are also

352 present from October in the models, but not in observations. A significant retreat of the

353 sea ice edge in the Barents Sea is also found for both models and observations in

354 October and November, which is also visible in December in the models.

355   The surface heat flux in lead and lag conditions can be used to discuss the

356 processes leading to the atmospheric circulation response. The heat flux preceding the

357 SCE is dominated by the atmospheric forcing of the snow cover, as for SST anomalies,

358 while the heat flux lagging the SCE should primarily reflect the heat flux directly forced

359 by the SCE (the thermodynamical component), although it could be strongly affected by

360 the surface heat flux intrinsically associated with the atmospheric response (hereafter

361 the dynamical heat flux component); at lag 0, both effects play a role and may even

362 cancel (Frankignoul et al. 1998). Since the surface heat flux responds rapidly to the

363 surface conditions (simultaneously on monthly timescale), one can use in-phase

364 relations to estimate the (thermodynamical) heat flux driven by the SCE anomalies, if

365 the (larger) dynamical component is removed. To do so, we first calculate the heat flux

366 by adding surface radiative and turbulent fluxes. A standardized atmospheric index,

367 referred to as ATM, was computed by projecting the November SLP anomalies over

368 30°N-90°N 80°W-180°E onto the SCA-like patterns shown in Fig. 4. The dynamical heat

15

369 flux component corresponding to one standard deviation of the MCA-snow index is

370 obtained by regressing the heat flux anomalies onto ATM, multiplied by the correlation

371 between ATM and MCA-snow (shown in Fig. S2). The total heat flux anomaly associated

372 with the SCE pattern in Fig. 3a is given by the regression of the heat flux onto MCA-snow

373 (shown in Fig. S3), while the difference of the two (Figs. 9a and 9b) is an estimate of the

374 thermodynamical effect. Figs. 9c-d show the net heat flux components integrated over

375 three boxes (see purple boxes in Fig. 9a-b) located over Siberia, Europe, and the Barents

376 and Kara Seas. The location of the boxes was adjusted to capture the snow and sea-ice

377 influences in models and observations.

378   In November, the heat flux changes induced by the snow cover are downward

379 over a wide latitudinal band in central Siberia from lake Balkhash to Sakhalin Island in

380 ERA-Interim and models (Fig. 9a-b), although the results are noisy in ERA-Interim. This

381 is consistent with a net cooling effect of positive snow cover anomalies, as the larger

382 surface albedo leads to more reflected shortwave radiation, and as the surface may be

383 more insulated from the warmer soil if the snow depth also increases (Orsolini et al.,

384 2016). The cooler surface temperature results in a dominant reduction of longwave

385 radiation and sensible heat flux. However, the turbulent fluxes have a larger

386 contribution in models, while the longwave and shortwave components dominate in

387 observations (Fig. 9c and 9d). Conversely, the heat flux anomalies are upward in ERA-

388 Interim over eastern Europe and Scandinavia where the SCE decreases, while in models,

389 there is almost no net heating effect. Interestingly, over the Barents-Kara Seas, the heat

390 flux is mainly upward over open-water in the Nordic Seas, which suggests a large

391 heating of the atmosphere where the sea ice has retreated in November. This is

392 consistent with an active influence of SIC anomalies onto the lower troposphere.

393 However, while the total heat flux release over the Barents-Kara Seas is dominant in

16

394   ERA-Interim, it is smaller and less robust in models. The same analysis applied to the

395   December heat flux provides comparable results over Europe and Siberia (see Fig. S4),

396   but the heating over the Barents-Kara Seas is larger in models, while a net cooling is

397   obtained in observations. This is because the sea-ice anomalies persist in December in

398   models (see Fig. 8f), while they vanish in ERA-Interim (Fig. 8e).

399   In summary, the diabatic forcing of SCE anomalies is consistent in models and

400   ERA-Interim, with cooling when the SCE increases. However, the diabatic heating from

401   the SIC anomalies over the Barents-Kara Seas is larger but it is also less robust than the

402   one associated with SCE. As the surface heat flux anomalies are not assimilated in ERA-

403   Interim and largely depend on the model physics, these results might be model

404   dependent.

405

406   *c. Troposphere-stratosphere coupling*

407   We calculated the regressions of the SLP (Fig. 10), zonal-mean temperature and

408   geopotential height (Fig. 11) onto November MCA-snow, from October to January. In

409   observations, the November SCE anomalies are preceded in October by a small

410   anticyclone centered over the northern coast of Siberia (Fig. 10a), as in Cohen et al.

411   (2002). In November, one month later, the SCA pattern (Fig. 10c) is visible, with cold

412   tropospheric anomalies over Eurasia between 40°N and 60°N, above the positive SCE

413   anomalies, and warm tropospheric anomalies at 78°N, at the location of the Barents-

414   Kara Seas (Fig. 4). The zonal mean anomalies are largely barotropic below 300-hPa,

415   which illustrates the main role of the tropospheric eddies in settling the SCA pattern.

416   The anomalous anticyclone over Eurasia has been interpreted as a response to October

417   Siberian snow cover, the snow-induced cooling acting to reinforce and expand westward

418   the Siberian High (Cohen et al., 2007; Jeong et al., 2011; Orsolini et al., 2013). However, it

419   can also be interpreted as a result of the stationary Rossby wave induced by the

420   anomalous turbulent heat flux from the sea ice retreat in the Barents-Kara Seas (e.g.

421   Honda et al. 2009; Garcia-Serrano et al. 2015), or as internal atmospheric variability

422   since simultaneous relations primarily show the SCE forcing by the SCA. In the lower

423   stratosphere, there is a warming over the polar cap (75°N-90°N, between 300-hPa and

424   100-hPa) and positive geopotential height anomalies above (Fig. 11a) that depicts a

425   weakening of the polar vortex. In December, one month later, a barotropic negative

426   NAO/AO pattern appears in the Euro-Atlantic region (Fig. 10e), while the polar vortex is

427   further weakened, with stratospheric temperature anomalies above 100 hPa that are

428   only significant between 40°N and 65°N (Fig. 11c). The regressions are similar in

429   January, with the SLP anomalies projecting on the AO (Fig. 10g), and stronger zonal-

430   mean geopotential height and temperature anomalies (Fig. 11e).

431   In the CMIP5 models, the atmospheric anomalies in October (Fig. 10b), which

432   precedes by one month the SCE anomalies, show alternating trough and ridges from the

433   North Atlantic to south-eastern Asia, with anticyclonic anomalies over the Urals and a

434   depression over Northern Europe, clearly indicative of a stationary wave and already

435   reminiscent of the SCA pattern. In November, the anomalies are more complex and

436   larger, with a dominant anticyclonic circulation over the Urals extending into the Arctic

437   (Fig. 10d), so that the Siberian High is clearly intensified and shifted westward, while the

438   SLP response is AO-like in December and, to a lesser extent, in January. The temperature

439   anomalies show a large warming in the lower troposphere north of 70°N (Fig. 11b, d)

440   from November to December, and display an important warming in the polar

441   stratosphere that persists into January only in the lowermost stratosphere at 200-hPa.

442   The warm anomalies are rather baroclinic in the polar troposphere, which is consistent

443   the influence of Arctic SIC reduction noted in Cattiaux and Cassou (2013). In November

444 and December, there are also cold temperature anomalies below 400-hPa south of the

445 positive SCE anomalies, likely associated with the cold temperature found over Siberia

446 where the snow cover increases (Fig. 10b,d). In models, both the tropospheric NAO/AO

447 pattern and the anomalies in the stratosphere are smaller during January, but they are

448 still significant (Fig. 10h and 11f).

449   The troposphere-stratosphere coupling is further illustrated by the polar cap

450 temperature (65°N-90°N) regression onto the MCA-snow index in Fig. 12. For

451 observations, the daily air temperature was used, while only monthly data was available

452 for models. The observations show a warming in the lower stratosphere between 200-

453 hPa and 70-hPa from December to February, as found by Cohen et al. (2014b) and

454 Orsolini et al. (2016), but it is only 10% significant for a few days in early December and

455 January. There are also hints of downward propagation in late December and late

456 January. In models the polar cap temperature anomalies are only half the ones observed,

457 the timing is different as the warming starts in November, one month earlier, and the

458 downward propagation is faster in the stratosphere with little penetration into the

459 troposphere.

460   In summary, the diabatic heating from the November SCE and, possibly, SIC

461 anomalies is associated with a stationary wave pattern that weakens the polar vortex.

462 Particularly in observations, the AO changes obtained one and two months later are

463 consistent with the downward propagation of polar vortex weakening. Next, we will

464 establish the relative importance of the SIC and snow cover anomalies.

465

466   *d. Link with sea ice anomalies*

467   In order to compare the role of SIC and SCE, we also perform a MCA using SIC

468 over the Barents-Kara Sea (65°N-85°N; 15°E-100°E) in November and SLP in December.

19

469   We additionally perform a MCA using both November SIC and SCE concatenated into a

470   single predictor field, with SLP as predictand field. The results are summarized in Table

471   2. When only using November SIC as predictor, the NSC is highly significant, but the

472   correlation R is lower than when using SCE, and not significant at the 10% level, as in

473   Garcia-Serrano et al. (2015; see also Fig. S5). On the other hand, using concatenated SCE

474   and SIC predictors is as significant as with SCE alone, and the MCA patterns (Fig. 13a)

475   show that the snow dipolar anomalies and the sea ice retreat in the Barents-Kara Seas

476   precede a negative AO-like pattern in December, which is consistent with previous

477   results (Fig. 8), but for larger SIC changes. Interestingly, SCE and SIC seem to contribute

478   similarly to the SLP response in Fig. 13. Indeed, projecting SIC anomalies onto the SIC

479   part of the MCA covariance map (referred to as MCAcat_SIC) and SCE anomalies onto the

480   SCE part (referred to as MCAcat_SCE) yields two well correlated time series (0.58,

481   significant at the 5% level) that compare well with the atmospheric December MCA time

482   series (Fig. 13b).

483   In order to evaluate the relative influence of the SCE and SIC pattern, we used the

484   time series associated with the SCE and SIC fields in the SCE/SLP (MCA-snow) and

485   SIC/SLP (referred to as MCA-SIC) individual MCA, respectively, to separate more clearly

486   the SIC and SCE influences. These two times series have a correlation of 0.42, and a

487   bivariate regression of the SLP using these two time series shows little multicollinearity

488   (variance inflation factor of 1.4). The regression slopes (Fig. 14) show that the SCE holds

489   a larger signal in observations, which is consistent with the higher correlation in the

490   MCA analysis (see Table 2). The SIC has a similar influence, but its amplitude is twice

491   smaller, and it is less significant. These results are not modified when using other

492   indices for SCE or SIC.

493   The concatenated MCA yields similar results for the four models, with a SCE

494   dipole and a decrease of SIC in November preceding the December AO (not shown),

495   although the NSC and correlation are much lower, and adding SIC to SCE (or considering

496   SIC alone) strongly degrades the significance (Table 2). Yet, the correlation between the

497   MCAcat_SCE and MCAcat_SIC time series (Table 3) is significant in each model, even if it

498   is lower than in observations, which can be explained by the different sampling, the

499   smaller SCA occurrence, or model biases such as the colder mean state in pre-industrial

500   climate, which allow less Barents-Kara SIC variability. However, these significance tests

501   are biased since the four models were selected based on their response to SCE, not to

502   SIC, and other CMIP5 models are more sensitive to SIC (Garcia-Serrano et al. 2016).

503   The same analysis was conducted using SIC anomalies in early autumn

504   (September or October) together with November SCE (Table S2), which provides

505   significant results only when using October SIC, with patterns as in Fig. 13, but smaller

506   NSC and R. We also repeated the analysis using November SIC/SCE and SLP in January

507   and February (Table S3), as the stratospheric pathway is also important during late

508   winter (Kim et al., 2014; Jaiser et al., 2016), but the MCA results are much less significant

509   in the observations.

510

511   *e. Link with the Scandinavian pattern*

512   The upward influence of tropospheric planetary waves into the stratosphere due

513   to atmospheric dynamics, such as during blocking situations, can also explain that the

514   SCA is followed by an AO-like pattern one month later, without any influence of surface

515   heating (Kuroda and Kodera, 1999; Takaya and Nakamura, 2008; Martius et al., 2009;

516   Woollings et al., 2010). To test the influence of such troposphere-stratosphere coupling,

517   we use an MCA with Eurasian SLP (0E-150E, 45N-85N), Eurasian SCE, and Barents/Kara

21

518   SIC in November concatenated as the predictor field, and Northern Hemisphere SLP in

519   December as the predictand field. For the sake of simplicity, the ENSO variability was

520   not removed in the analysis. In both observations and models, the results of this MCA

521   are strongly significant (Table 2), and the covariance maps are similar to Fig. 13, with

522   the homogeneous SLP covariance map in November resembling the SCA (not shown).

523   Time series of the three November predictors (SCE dipole, Barents/Kara SIC,

524   SCA) are then studied. The time series associated with the SCE and SIC fields are

525   obtained as before from the SCE/SLP (MCA-snow) and SIC/SLP (MCA-SIC) individual

526   MCAs, while the SCA index is given by the first rotated EOF of the Eurasian SLP (0E-

527   150E, 45N-85N) in November. To distinguish the impacts of each predictor, a

528   multivariate regression of the December SLP on the three predictors is done, noting that,

529   despite the large correlation between predictors, multicollinearity is limited (variance

530   inflation factors < 2.0). The results (Fig. 15a-c) again show that the SCE dipole has the

531   dominant influence onto SLP in December, while the SIC provides weaker, but

532   significant anomalies as in the bivariate regression in Fig. 14. The SCA seems to be also

533   important for the SLP over the British Isles or Alaska, but the anomalies are weaker and

534   not significant. A similar multivariate regression using an AO index, as given by the first

535   EOF of December SLP is shown in Fig. 15d. Again, the SCE appears to be the best

536   predictor of the AO, followed by the SIC, while the SCA has the lowest R^2. Taking the

537   three indices as predictors with a multivariate regression only slightly improves the

538   variance explained by the SCE alone. In the four models (Fig. 15d, symbols using the

539   right vertical axis), the same analysis also shows that the SCE dipole still plays the

540   dominant role in three models, while the SIC has a dominant influence only in one model

541   (CanESM). In all models, the SCA pattern also appears as good predictor of the AO. This

542   suggests that, in these models selected based on their response to SCE, internal

22

543   atmospheric dynamical processes may also explain the statistical relationship found

544   among SCE, SIC and the atmosphere one month later, hence that the influence of SCE and

545   SIC is underestimated. These conclusions are not substantially modified when using

546   other indices for the AO, the snow dipole or the Barents-Kara SIC anomalies.

547

548   **5. Discussions and Conclusion**

549   We have investigated the links between Eurasian SCE and the atmosphere in

550   observations during 1979-2014 and CMIP5 models. We found that a dipole of snow

551   cover anomalies in November with positive (negative) snow cover anomalies over

552   eastern Siberia (eastern Europe) leads to a negative AO one month later in December.

553   The largest statistical links are found when considering November SCE, as in Orsolini et

554   al. (2016), but other studies focus more on October snow cover (Cohen and Entekhabi,

555   1999; Cohen et al. 2007; Cohen and Jones 2011; Handorf et al. 2015). Lagged regression

556   actually reveals that the November SCE is related to similar anomalies in October, but

557   statistical significance is too limited with the MCA using October SCE. The choice of the

558   data set, the methodology and the period considered might explain this discrepancy (see

559   Appendix A). The CMIP5 models, in general, fail to simulate this potential effect of snow

560   cover. Nevertheless, a weaker, but similar, relationship between the SCE and the AO is

561   present in four models: CanESM, MPI-ESM-LR, GISS-E-R and CESM-BGC.

562   The models and ERA-Interim indicate that downward (upward) heat flux

563   anomalies are simulated over positive (negative) snow cover anomalies over Siberia

564   (Europe) during November. We verified that eastern Siberia pole of the snow dipole

565   anomalies has the best relationship with the AO one month later both in observations

566   and models, so that the SCE over Siberia seems to have the largest influence. The

567   diabatic cooling of the troposphere over Siberia is consistent with the intensification and

568   westward expansion of the Siberian High. This may lead to a polar vortex weakening

569   from November to January driven by upward planetary wave activity flux, as found

570   previously in observations (Saito et al. 2001; Handorf et al. 2015; Furtado et al. 2016)

571   and in sensitivity experiments using SCE anomalies (Gong et al., 2004; Fletcher et al.,

572   2009; Peings et al., 2012; Orsolini et al. 2013; Orsolini et al. 2016). Here, we show that

573   the same process can be verified qualitatively using multi-centennial control climate

574   model simulations, although the SCE influence is much weaker.

575   The atmospheric pattern responsible for the variability of the snow cover dipole

576   is the Scandinavian pattern (SCA, as in Bueh and Nakamura, 2007), with a large

577   anticyclone over the Urals. Such anticyclone leads to northerly cold advection east of the

578   anticyclone, bringing cold air over Siberia, and southerly warm advection over Central

579   Europe and the Barents and Kara Seas. The SCA forcing explains that the Barents/Kara

580   SIC and Eurasian snow cover are largely correlated (Wegmann et al., 2015; Furtado et

581   al., 2016). We find that the models produce less frequent SCA-like and more frequent

582   AO-like events, possibly linked to blocking processes that are not well simulated in low

583   resolution models (Dawson, 2012), but this could also be due to natural atmospheric

584   variability. Deficiencies in the simulation of the SCA characteristics in models might

585   therefore explain the weaker SCE influence in models. In addition, the upward heat flux

586   driven by a retreat of the sea ice cover in the Barents-Kara Seas is weaker and less

587   robust in the models than in ERA-Interim, perhaps explaining why the SIC influence is

588   also underestimated in the four models that simulate the SCE impacts.

589   A MCA using SLP and combined SCE and SIC suggests that November SCE and SIC

590   forcing provide similar covariability with the December AO in observations. However, a

591   bivariate regression reveals that the SCE dipole is a much better predictor than the

592   Barents-Kara SIC anomaly. As the SCE and the SIC variability are linked, both field can

24

593 constructively interfere to weaken the polar vortex, as suggested in Cohen et al. (2014a),

594 although the surface forcing from the snow cover anomalies might be dominant. On the

595 other hand, the November SIC in models has an impact on the AO in only one model,

596 perhaps because they were selected based on their representation of the SCE influence.

597 When investigating more systematically the links between Greenland-Barents-Kara SIC

598 and the NAO/AO in most CMIP5 models, Garcia-Serrano et al. (2016) did find a robust

599 SIC influence, but they noted that the timing or the processes for the SIC influence are

600 model dependent. Here, the lack of links between November SIC and December

601 atmosphere may result from our selection of the models based on their representation

602 of the SCE impact (and not SIC impact), and also from the model averaging that may mix

603 different behavior among models. The weaker SCE influence in models and the lack of

604 link between the SCE and SIC is consistent with the underestimated troposphere-

605 stratosphere coupling in models, as found in Furtado et al. (2015). However, it can also

606 be explained by the poor simulation of the SCA, the colder climate in preindustrial

607 control simulation, or natural climate variability.

608   A better understanding of the coupling between land snow cover, Arctic sea ice,

609 and the atmosphere using dedicated climate model experiments would be necessary to

610 properly assess the causality links and better discriminate between their influence on

611 the winter AO. Nonetheless, the methodology used here could be applied to climate

612 projection of the 21st century in order to investigate how the polar amplification of

613 global warming will modify the links between the atmosphere and Arctic surface

614 conditions.

615

616

617

Appendix : October snow cover influence

The influence of October SCE on the atmosphere is discussed by using the MCA results, when SLP lags by one month, although statistical significance is limited (see Fig. 1). The covariance maps (Fig. A1a) show that increasing October SCE over northern Eurasia precedes a SLP pattern in November that has some resemblance with the SCA, plus a deeper Aleutian low. This differs from the negative AO found later, from December to February. It might be due the snow data used, as many previous studies used a more integrated snow index, such as the Eurasian snow cover areal extent (e.g. Cohen et al. 2007; Cohen and Fletcher 2007). It could be due to differences in methodology, as Furtado et al. (2016) used multivariate EOF. It could also be due to non-stationarity (Peings et al., 2013). For instance, Cohen et al. (2007) considered the 1948-2004 period, Cohen and Fletcher (2007) the 1972-2005 one, while we focus on 1979-2014.

To investigate the possible influence of non-stationarity, we performed the MCA in different sub-periods (Table A1). The most significant influence of October snow cover on SLP is found for November in the 1979-2005 period, as used in Cohen and Fletcher (2007); the MCA mode is also significant for December SLP, with a MCA pattern (Fig. A1d) sharing a large similarity with previous studies (i.e. Handorf et al., 2015). However, the levels of significance are limited when the DJF atmosphere is considered. If 1979-2011 or 1979-2014 is used, significance is lost. Hence, the detected influence of the October snow cover is sensitive to the period.

References

656

657 Allen, R. J., and C. S. Zender, 2010. Effects of continental-scale snow albedo anomalies on

658 the wintertime Arctic oscillation. *J. Geophys. Res. Atmos.*, **115**, D23105,

659 doi:10.1029/2010JD014490.

660 Barnett, T. P., L. Dümenil, U. Schlese, E. Roeckner, and M. Latif, 1989. The effect of

661 Eurasian snow cover on regional and global climate variations. *J. Atmos. Sci.*, **46**, 661–

662 686.

663 Barnston, A. G., and R. E. Livezey, 1987. Classification, seasonality and persistence of

664 low-frequency atmospheric circulation patterns. *Mon. Weather Rev.*, **115**, 1083–1126.

665 Bretherton, C. S., C. Smith, and J. M. Wallace, 1992. An intercomparison of methods for

666 finding coupled patterns in climate data. *J. Clim.*, **5**, 541–560.

667 Bueh, C., and H. Nakamura, 2007. Scandinavian pattern and its climatic impact. *Q. J. R.*

668 *Meteorol. Soc.*, **133**, 2117–2131.

669 Cattiaux, J., and C. Cassou, 2013. Opposite CMIP3/CMIP5 trends in the wintertime

670 Northern Annular Mode explained by combined local sea ice and remote tropical

671 influences. *Geophys. Res. Lett.*, **40**, 3682-3687, doi:10.1002/grl.50643.

672 Cattiaux, J., H. Douville, and Y. Peings, 2013. European temperatures in CMIP5: origins of

673 present-day biases and future uncertainties. *Clim. Dyn.*, **41**, 2889-2907.

674 Close, S., M.-N Houssais, and C. Herbaut, 2015. Regional dependence in the timing of

675 onset of rapid decline in Arctic sea ice concentration. *J. Geophys. Res. Ocean.*, **120**, 8077–

676 8098*,* doi:10.1002/2015JC011187*.*

677 Cohen, J., 1994. Snow cover and climate. *Weather*, **49**, 150-156.

28

678   Cohen, J. L., J. C. Furtado, M. A. Barlow, V. A. Alexeev, and J. E. Cherry, 2012. Arctic

679   warming, increasing snow cover and widespread boreal winter cooling. *Environ. Res.*

680   *Lett.*, **7**, 14007.

681   Cohen, J., and D. Entekhabi, 1999. Eurasian snow cover variability and Northern

682   Hemisphere climate predictability. *Geophys. Res. Lett.*, *26*(3), 345–348,

683   doi :10.1029/1998GL900321.

684   Cohen, J., and C. Fletcher, 2007. Improved skill of Northern Hemisphere winter surface

685   temperature predictions based on land-atmosphere fall anomalies. *J. Clim.*, **20**, 4118–

686   4132.

687   Cohen, J., and J. Jones, 2011. A new index for more accurate winter predictions. *Geophys.*

688   *Res. Lett*, **38***, L21701, doi:10.1029/2011GL049626.

689   Cohen, J., M. Barlow, P. J. Kushner, and K. Saito, 2007. Stratosphere-troposphere

690   coupling and links with Eurasian land surface variability. *J. Clim.*, **20**, 5335–5343.

691   Cohen, J., D. Salstein, and K. Saito, 2002. A dynamical framework to understand and

692   predict the major Northern Hemisphere mode. *Geophys. Res. Lett.*, **29**(10)*,

693   doi:10.1029/2001GL014117.

694   Cohen, J., and Coauthors, 2014a. Recent Arctic amplification and extreme mid-latitude

695   weather. *Nat. Geosc.*, **7**(9), 627–637.

696   Cohen, J., Furtado, J. C., Jones, J., Barlow, M., Whittleston, D., and Entekhabi, D., 2014b.

697   Linking Siberian snow cover to precursors of stratospheric variability. *J. Clim.*, **27**, 5422-

698   5432.

699   Comiso, J. C., 2012. Large decadal decline of the Arctic multiyear ice cover. *J. Clim.*, **25**,

700   1176–1193.

701   Czaja, A., and C. Frankignoul, 2002. Observed impact of Atlantic SST anomalies on the

702   North Atlantic Oscillation. *J. Clim.*, **15**, 606–623.

703   Dawson, A., T. N. Palmer, and S. Corti, 2012. Simulating regime structures in weather and

704   climate prediction models. *Geophys. Res. Lett.*, **39***,* L21805, doi:10.1029/2012GL053284*.*

705   Dee, D. P. and Coauthors, 2011. The ERA-Interim reanalysis: Configuration and

706   performance of the data assimilation system. *Q. J. R. Meteorol. Soc.*, **137**, 553–597.

707   Déry, S. J., and R. D. Brown, 2007. Recent Northern Hemisphere snow cover extent

708   trends and implications for the snow-albedo feedback. *Geophys. Res. Lett.*, **34***,* L22504,

709   doi:10.1029/2007GL031474.

710   Deser, C., G. Magnusdottir, R. Saravanan, and A. Phillips, 2004. The effects of North

711   Atlantic SST and sea ice anomalies on the winter circulation in CCM3. Part II: Direct and

712   indirect components of the response. *J. Clim.*, **17**, 877–889.

713   Deser, C., R. A. Tomas, and S. Peng, 2007. The transient atmospheric circulation response

714   to North Atlantic SST and sea ice anomalies. *J. Clim.*, **20**, 4751–4767.

715   Dutra, E.*,* S. Kotlarski*,* P. Viterbo*,* G. Balsamo*,* P. M. A. Miranda*,* C. Schär*,* P. Bissolli*,* and T.

716   Jonas, 2011. Snow cover sensitivity to horizontal resolution, parameterizations, and

717   atmospheric forcing in a land surface model*, J. Geophys. Res.,* **116***, D21109,*

718   doi:10.1029/2011JD016061*.*

719   Fasullo, J. (2004). A stratified diagnosis of the Indian monsoon-Eurasian snow cover

720   relationship. *J. Clim.*, **17**, 1110–1122.

721   Fletcher, C. G., S. C. Hardiman, P. J. Kushner, and J. Cohen, 2009. The dynamical response

722   to snow cover perturbations in a large ensemble of atmospheric GCM integrations. *J.*

723   *Clim.*, **22**, 1208-1222.

724   Fletcher, C. G., P. J. Kushner, and J. Cohen, 2007. Stratospheric control of the extratropical

725   circulation response to surface forcing. *Geophys. Res. Lett*, **34***,* L21802,

726   doi:10.1029/2007GL031626.

727   Francis, J. A., W. Chan, D. J. Leathers, J. R. Miller, and D. E. Veron, 2009. Winter Northern

728   Hemisphere weather patterns remember summer Arctic sea-ice extent. *Geophys. Res.*

729   *Lett.*, **36**, L07503, doi:10.1029/2009GL037274.

730   Frankignoul, C., A. Czaja, and B. L'Heveder, 1998. Air-sea feedback in the North Atlantic

731   and surface boundary conditions for ocean models. *J. Clim.*, **11**, 2310-2324.

732   Frankignoul, C., N. Sennéchael, and P. Cauchy, 2014. Observed atmospheric response to

733   cold season sea ice variability in the Arctic. *J. Clim.*, **27**, 1243–1254.

734   Frankignoul, C., N. Sennéchael, Y.-O. Kwon, and M. A. Alexander, 2011. Influence of the

735   meridional shifts of the Kuroshio and the Oyashio Extensions on the atmospheric

736   circulation. *J. Clim.*, **24**, 762–777.

737   Furtado, J. C., J. L. Cohen, and E. Tziperman, 2016. The Combined Influences of Autumnal

738   Snow and Sea Ice on Northern Hemisphere Winters. *Geophys. Res. Lett.*, **43**, 3478–3485,

739   doi:10.1002/2016GL068108.

740   Furtado, J. C., J. L. Cohen, A. H. Butler, E. E. Riddle, and A. Kumar, 2015. Eurasian snow

741   cover variability and links to winter climate in the CMIP5 models. *Clim. Dyn.*, **45**, 2591–

742   2605.

743   García-Serrano, J., C. Frankignoul, G. Gastineau, and A. De La Càmara, 2015. On the

744   predictability of the winter Euro-Atlantic climate: lagged influence of autumn Arctic sea

745   ice. *J. Clim.*, **28**, 5195–5216.

746   García-Serrano, J. and Coauthors, 2016. Multi-model assessment of linkages between

747   eastern Arctic sea-ice variability and the Euro-Atlantic atmospheric circulation in

748   current climate. *Clim. Dyn.*, doi :10.1007/s00382-016-3454-3.

749   Gastineau, G., and C. Frankignoul, 2015. Influence of the North Atlantic SST variability on

750   the atmospheric circulation during the twentieth century. *J. Clim.*, **28**, 1396-1416.

31

751 Gong, G., D. Entekhabi, J. Cohen, and D. Robinson, 2004. Sensitivity of atmospheric

752 response to modeled snow anomaly characteristics. *J. Geophys. Res. Atmos.*, **109**, D06107,

753 doi:10.1029/2003JD004160.

754 Handorf, D., R. Jaiser, K. Dethloff, A. Rinke, and J. Cohen, 2015. Impacts of Arctic sea ice

755 and continental snow cover changes on atmospheric winter teleconnections. *Geophys.*

756 *Res. Lett*, *42*(7), 2367–2377, doi: 10.1002/2015GL063203.

757 Honda, M., J. Inoue, and S. Yamane, 2009. Influence of low Arctic sea-ice minima on

758 anomalously cold Eurasian winters. *Geophys. Res. Lett*, **36**, L08707,

759 doi:10.1029/2008GL037079.

760 Hurrell, J. W., 1995. Decadal trends in the North Atlantic Oscillation: regional

761 temperatures and precipitation. *Science*, **269**(5224), 676–679.

762 Jaiser, R., T. Nakamura, D. Handorf, K. Dethloff, J. Ukita, and K. Yamazaki, 2016.

763 Atmospheric winter response to Arctic sea ice changes in reanalysis data and model

764 simulations. *J. Geophys. Res. Atmos.*, **121**, 7564-7577, doi:10.1002/2015JD024679.

765 Jeong, J.-H., T. Ou, H. W. Linderholm, B.-M. Kim, S.-J. Kim, J.-S. Kug, and D. Chen, 2011.

766 Recent recovery of the Siberian High intensity, *J. Geophys. Res.*, **116**, D23102,

767 doi:10.1029/2011JD015904.

768 Jeong, J. H., H. W. Linderholm, S. H. Woo, C. Folland, B. M. Kim, S. J. Kim and D. Chen,

769 2013. Impacts of snow initialization on subseasonal forecasts of surface air temperature

770 for the cold season. *J. Clim.*, **26**, 1956-1972.

771 Kaiser, H. F., 1958: The Varimax criterion for analytic rotations infactor analysis.

772 *Psychometrika*, **23**,187–200.

773 Kim, B.-M., S.-W. Son, S.-K. Min, J.-H. Jeong, S.-J. Kim, X. Zhang, T. Shim and J.-H. Yoon,

774 2014. Weakening of the stratospheric polar vortex by Arctic sea-ice loss. *Nat. Comm.*, **5**,

775 4646.

776 King, M. P., M. Hell, and N. Keenlyside, 2016. Investigation of the atmospheric

777 mechanisms related to the autumn sea ice and winter circulation link in the Northern

778 Hemisphere. *Clim. Dyn.*, **46**, 1185-1195.

779 Koenigk, T., M. Caian, G. Nikulin, and S. Schimanke, 2016. Regional Arctic sea ice

780 variations as predictor for winter climate conditions. *Clim. Dyn.*, **46**, 317–337.

781 Kuroda, Y., and K. Kodera, 1999. Role of planetary waves in the stratosphere-

782 troposphere coupled variability in the northern hemisphere winter. *Geophys. Res. Lett*,

783 **26**, 2375–2378, doi:10.1029/1999GL900507.

784 Luo, D., Y. Xiao, Y. Yao, A. Dai, I. Simmonds, and C. L. Franzke, 2016. Impact of Ural

785 Blocking on Winter Warm Arctic–Cold Eurasian Anomalies. Part I: Blocking-Induced

786 Amplification. *J. Clim.*, **29**, 3925-3947.

787 Magnusdottir, G., C. Deser, and R. Saravanan, 2004. The effects of North Atlantic SST and

788 sea ice anomalies on the winter circulation in CCM3. Part I: Main features and storm

789 track characteristics of the response. *J. Clim.*, **17**, 857–876.

790 Martius, O., L. M. Polvani, and H. C. Davies, 2009. Blocking precursors to stratospheric

791 sudden warming events. *Geophys. Res. Lett.*, **36**, L14806, doi:10.1029/2009GL038776.

792 Nakamura, T., K. Yamazaki, K. Iwamoto, M. Honda, Y. Miyoshi, Y. Ogawa, and J. Ukita,

793 2015. A negative phase shift of the winter AO/NAO due to the recent Arctic sea-ice

794 reduction in late autumn. *J. Geophys. Res. Atmos.*, **120**, *3209–3227,*

795 *doi:10.1002/2014JD022848.*

796 Nakamura, T., K. Yamazaki, K. Iwamoto, M. Honda, Y. Miyoshi, Y., Ogawa, Y. Tomikawa

797 and J. Ukita, 2016. The stratospheric pathway for Arctic impacts on midlatitude climate.

798 *Geophys. Res. Lett*, **43**, 3494-3501, doi:10.1002/2016GL068330.

799   Orsolini, Y. J., R. Senan, G. Balsamo, F. J. Doblas-Reyes, F. Vitart, A. Weisheimer, A.

800   Carrasco, R. E. Benestad, 2013. Impact of snow initialization on sub-seasonal forecasts.

801   *Clim. Dyn.*, **41**, 1969–1982, doi :10.1007/s00382-013-1782-0.

802   Orsolini, Y. J., R. Senan, F. Vitart, G. Balsamo, A. Weisheimer and F. J. Doblas-Reyes, 2016.

803   Influence of the Eurasian snow on the negative North Atlantic Oscillation in subseasonal

804   forecasts of the cold winter 2009/2010. *Clim. Dyn.*, **47**, 1325–1334,

805   doi :10.1007/s00382-015-2903-8.

806   Overland, J., J. A. Francis, R. Hall, E. Hanna, S.-J. Kim, and T. Vihma, 2015. The Melting

807   Arctic and Midlatitude Weather Patterns: Are They Connected? *J. Clim.*, **28**, 7917–7932.

808   Peings, Y., and H. Douville, 2010. Influence of the Eurasian snow cover on the Indian

809   summer monsoon variability in observed climatologies and CMIP3 simulations. *Clim.*

810   *Dyn.*, **34**, 643–660.

811   Peings, Y., E. Brun, V. Mauvais, and H. Douville, 2013. How stationary is the relationship

812   between Siberian snow and Arctic Oscillation over the 20th century? *Geophys. Res. Lett*,

813   **40**, 183–188, doi:10.1029/2012GL054083.

814   Peings, Y., H. Douville, R. Alkama, and B. Decharme, 2011. Snow contribution to

815   springtime atmospheric predictability over the second half of the twentieth century.

816   *Clim. Dyn.*, **37**, 985-1004.

817   Peings, Y., D. Saint-Martin, and H. Douville, 2012. A numerical sensitivity study of the

818   influence of Siberian snow on the northern annular mode. *J. Clim.*, **25**, 592-607.

819   Petoukhov, V., and V. A. Semenov, 2010. A link between reduced Barents-Kara sea ice

820   and cold winter extremes over northern continents. *J. Geophys. Res.*, **115***, D21111,

821   doi:10.1029/2009JD013568*.

822   Riddle, E. E., A. H. Butler, J. C. Furtado, J. L. Cohen, and A. Kumar, 2013. CFSv2 ensemble

823   prediction of the wintertime Arctic Oscillation. *Clim. Dyn.*, **41**, 1099–1116.

824   Saito, K., J. Cohen, and D. Entekhabi, 2001. Evolution of atmospheric response to early-

825   season Eurasian snow cover anomalies. *Mon. Weather Rev.*, **129**, 2746–2760.

826   Saito, K.*,* and J. Cohen, 2003. The potential role of snow cover in forcing interannual

827   variability of the major Northern Hemisphere mode*, Geophys. Res. Lett.,* **30***, 1302,*

828   doi:10.1029/2002GL016341*.*

829   Scaife, A. A., and Coauthors, 2014. Skillful long-range prediction of European and North

830   American winters. *Geophys. Res. Lett*, **41**, 2514–2519, doi:10.1002/2014GL059637.

831   Seviour, W. J. M.*,* L. J. Gray, and D. M. Mitchell, 2016. Stratospheric polar vortex splits

832   and displacements in the high-top CMIP5 climate models*. J. Geophys. Res. Atmos.,* **121***,*

833   1400–1413*,* doi:10.1002/2015JD024178*.*

834   Smoliak, B. V., and J. M. Wallace, 2015. On the Leading Patterns of Northern Hemisphere

835   Sea Level Pressure Variability. *J. Atmos. Sci.*, **72**, 3469–3486.

836   Takaya, K., and H. Nakamura, 2008. Precursory changes in planetary wave activity for

837   midwinter surface pressure anomalies over the Arctic. *J. Meteorol. Soc. Japan. Ser. II*, **86**,

838   415–427.

839   Vautard, R., 1990. Multiple weather regimes over the North Atlantic: Analysis of

840   precursors and successors. *Mon. Weather Rev.*, **118**, 2056–2081.

841   Wegmann, M and Coauthors, 2015. Arctic moisture source for Eurasian snow cover

842   variations in autumn. *Environ. Res. Lett.*, **10**, 054015, doi:10.1088/1748-

843   9326/10/5/054015.

844   Woollings, T., A. Charlton-Perez, S. Ineson, A. G. Marshall, and G. Masato, 2010.

845   Associations between stratospheric variability and tropospheric blocking. *J. Geophys.*

846   *Res.,* **115**, D06108, doi:10.1029/2009JD012742.

847   Wu, Q., and X. Zhang, 2010. Observed forcing-feedback processes between Northern

848   Hemisphere atmospheric circulation and Arctic sea ice coverage. *J. Geophys. Res.,* **115**,

849   D14119, doi:10.1029/2009JD013574.

850   Yamamoto, K., Y. Tachibana, M. Honda, and J. Ukita, 2006. Intra-seasonal relationship

851   between the Northern Hemisphere sea ice variability and the North Atlantic Oscillation.

852   *Geophys. Res. Lett*, **33**, L14711*, doi:*10.1029/2006GL026286*.*

853   Zhang, Y., T. Li, and B. Wang, 2004. Decadal change of the spring snow depth over the

854   Tibetan Plateau: the associated circulation and influence on the east Asian summer

855   monsoon. *J. Clim.*, **17**, 2780–2793.

856

Tables

TABLE 1. CMIP5 models and control simulations used.

	Group	Model	AGCM Resolution	length (year)
1	CCCma	CanESM2	2.8°x2.8° L35	995
2	CNRM-CERFACS	CNRM-CM5	1.4°x1.4° L31	850
3	CSIRO-QCCCE	CSIRO-Mk3-6-0	1.9°x1.9° L18	500
4	LASG-CESS	FGOALS-g2	2.8°x2.8° L26	700
5	MIROC	MIROC-ESM	1.4°x1.4° L40	630
6	MPI-M	MPI-ESM-LR	1.9°x1.9° L47	1000
7	MRI	MRI-CGCM3	1.1°x1.1° L48	500
8	NASA-GISS	GISS-E2-R	2.5°x2° L40	550
9	NCAR	CCSM4	1.25°x0.9° L26	600
10	NCC	NorESM1-ME	2.5°x1.9° L26	250
11	NSF-DOE-NCAR	CESM1-BGC	1.25°x0.9° L26	500
12	IPSL	IPSL-CM5A-LR	1.9°x3.75° L39	1000

857
858
859
860
861
862

863

864   TABLE 2. Statistics of different MCAs using December SLP as the left field, and November

865   snow cover (SCE), SIC, concatenated SCE and SIC (SCE+SIC) or concatenated SCE, SIC

866   and Eurasian SLP (SCE+SIC+SLP$_{Eur}$) as the right field. For the models, the mean over the

867   four selected models is given. The level of significance is given in parenthesis for

868   observation (see section 2c for details). For climate models, the number in parenthesis

869   indicates the number of models, out of four, where the level of significance is equal or

870   below 10%.

871

	OBS		Models	
	NSC	R	NSC	R
SCE	2.5 (0%)	0.82 (1%)	0.10 (4/4)	0.23 (4/4)
SIC	2.9 (3%)	0.61 (18%)	0.14 (1/4)	0.14 (1/4)
SCE+SIC	2.4 (0%)	0.75 (2%)	0.10 (2/4)	0.16 (0/4)
SCE+SIC+SLP$_{Eur}$	2.1 (0%)	0.78 (0%)	0.14 (4/4)	0.24 (4/4)

872

873

874

875

876

877   TABLE 3. Correlation between MCAcat-SCE and MCAcat-SIC time series. The bold

878   numbers indicate 1% significance.

879

Data	Correlation
Observations	**0.58**
CanESM2	**0.26**
GISS-E2-R	**0.24**
MPI-ESM-LR	**0.40**
CESM1-BGC	**0.27**

880

881

882   TABLE A1. Statistics of the MCA using October snow cover and SLP in following months,

883   using different time periods (79-05 : from 1979 to 2005 ; 79-11 : from 1979 to 2011 and

884   79-14 : from 1979 to 2014), and atmospheric months (NOV : November ; DEC :

885   December ; DJF : December-January-February). The level of statistical significance is

886   given in parenthesis.

887

Period	SLP season	NSC	R
79-14	NOV	1.3 (10%)	0.70 (13%)
79-14	DJF	1.1 (29%)	0.63 (32%)
79-05	NOV	1.9 (3%)	0.83 (5%)
79-05	DEC	1.9 (6%)	0.80 (6%)
79-05	DJF	2.4 (6%)	0.71 (25%)
79-11	NOV	1.1 (27%)	0.77 (21%)
79-11	DEC	1.6 (9%)	0.71 (27%)
79-11	DJF	1.5 (11%)	0.66 (44%)

888

889

890

Figures Caption

892 **Figure 1** :

893 Normalized squared covariance (NSC, contours, in %) for the first MCA mode between

894 observed SLP and Eurasia snow cover, for each month in the atmosphere. The lag is

895 positive when the snow cover leads SLP. The gray shade provides the level of statistical

896 significance for NSC. The plus symbols indicate the atmospheric month and time lag

897 where the level of significance for the correlation (R) is below 5%.

898

899 **Figure 2** :

900 (a) Scatter plot of the confidence level, in %, of the normalized squared covariance, NSC,

901 versus that of the correlation, R, for the first MCA mode between SLP and Eurasian snow

902 cover. (b) Scatter plot of the spatial correlation between the SLP covariance map found

903 in models and that of ERA-Interim, versus the spatial correlation between the snow

904 cover covariance map found in models and that of ERA-Interim. The black indicates the

905 results for SLP in December and SCE in November (one month lag). The blue indicates

906 the results for SLP in November and SCE in October (one month lag). The red indicates

907 the results for the SLP in January and SCE in November (two month lag). In (b), the bold

908 symbols indicate levels of significance lower than 15% for both NSC and R.

909

910 **Figure 3** :

911 (a) Homogeneous snow cover fraction (in %) and heterogeneous SLP (in hPa)

912 covariance maps for the first MCA mode, for December SLP and November snow cover,

913 when the snow cover leads by one month the atmosphere, in ERA-Interim. (b) Same as

914   (a), but using January SLP with a 2 month lag. (c), (d), (e), (f) and (g) same as (a) but for

915   CanESM2, MPI-ESM, GISS-E2-R, CESM1-BGC and the mean of the four models,

916   respectively. Note that the color scale is different for observation and models. (h) Box

917   plots of the NSC and R statistics from the MCA using 36-yr periods extracted from the

918   control runs of each models (1: CanESM2, 2:MPI-ESM, 3: GISS-E2-T and 4: CESM1-BGC),

919   error bars show the 5% and 95% percentiles. The dashed horizontal lines show the NSC

920   and R values in observations.

921

922   **Figure 4** :

923   Regression of SLP (contours, in hPa) and 2m air temperature, (color, in K) on the MCA-

924   snow index, in November, for (a) ERA-Interim and (b) the subset of four models. In (a),

925   colors are masked if the level of significance is above 10% for observation. In (b), colors

926   indicate anomalies of the same sign among the four models.

927

928   **Figure 5** :

929   Homogeneous SLP (in hPa) and heterogeneous snow cover (in %) covariance maps for

930   the first MCA mode, when the SLP and snow cover are simultaneous (no lag), for (a)

931   November fields in ERA-Interim; (b) December fields in ERA-Interim and (c) November

932   fields in the mean of the four models subset.

933

934   **Figure 6** :

935   (a) REOF1 of November SLP (in hPa) in ERA-Interim. (b) Same as (a) for the model mean

936   REOF1 using the four models. In (a), the variance fraction is given in parenthesis. In (b),

937   the minimum and maximum variance fraction among the four models is indicated in

938   parenthesis. (c) Box plots of the November variance (in %) explained by the SCA and the

939   NAO/AO in 36-yr chunks from the control runs of each models (1: CanESM2, 2:MPI-ESM,

940   3: GISS-E2-R and 4: CESM1-BGC); the error bars give the 5% and 95% percentiles, and

941   the dashed horizontal lines the AO and SCA variance fraction in observations.

942

943   **Figure 7** :

944   Regression of the December SLP in hPa onto (Left) European and (Right) Siberian snow

945   anomalies, given by multivariate regression; for (upper) ERA-Interim and (lower) the

946   subset of four models. In (a) and (b), colors are masked if the level of statistical

947   significance is above 10%. In (c) and (d), colors indicate anomalies of the same sign

948   among the four models.

949

950   **Figure 8** :

951   Regression of the snow cover fraction (color shades over continent, in %) and sea ice

952   concentration (blue contours and shades over the ocean, in %), onto the November

953   MCA-snow index, for (a) ERA-Interim in October; (b) the four models in October; (c) and

954   (d) Same as (a) and (b) for November; (e) and (f) same as (a) and (b) for December. The

955   sea-ice concentration contour interval is 5% in observations, and 1% for models, the

956   zero contour is removed. The thick gray contour provides the 50% contour for

957   climatological SIC.

958

959   **Figure 9** :

960   Thermodynamical component of the heat flux, positive upward, in W m^{-2}, associated in

961   November with the November MCA-snow index in (a) ERA-Interim and (b) the four

962   models. The color scale is different over land and ocean to emphasize the changes over

963   continental surfaces. Note the different contour intervals for ERA-Interim and models.

964   (c,d) Regressions of the shortwave (SW), longwave (LW), sensible (SH), latent (LH) and

965   total (Tot) heat flux over the Siberia (SIB), Europe (EUR) and Barents-Kara Sea (B/K)

966   integrated over boxes shown in (a) and (b) with histograms for (c) ERA-Interim and (d)

967   the four models mean. In (d) the error bars indicate the minimum and maximum values

968   among models.

969

970   **Figure 10** :

971   Regression of the SLP, in hPa (contour interval 0.5 hPa), onto the MCA-snow index, (left

972   column) ERA-Interim and (right column) models, in (a), (b) October; (c), (d) November;

973   (e), (f) December and (g), (h) January . The thick black line indicates 5% significance for

974   observations or anomalies of the same sign among the four models. The contour interval

975   at -0.2 and 0.2 hPa was added for models.

976

977   **Figure 11** :

978   Regression of the zonal-mean temperature (gray contours and color shades, in K) and

979   geopotential height (blue contours, in m) onto the MCA-snow normalized index, for (left

980   column) ERA-Interim and (right column) models, in (a), (b) November; (c), (d)

981   December and (e), (f) January. Colors indicate zonal mean temperature (left) level of

982   significance below 10% or (right) anomalies of the same sign among the four models.

983

984   **Figure 12** :

985   Regression of the temperature over the polar cap (65°N-90°N) onto the MCA-snow

986   normalized index, for (a) ERA-Interim and (b) models. The thick black lines indicate (a)

987   level of significance below 10% or (b) anomalies of the same sign among the four

988   models. Note the different contour intervals.

989

Figure 13 :

 (a) Snow cover (color over land, in %) and SIC (color over ocean, in %) homogeneous

covariance map and SLP (in hPa) heterogeneous map for the first MCA mode using

combined snow/sea-ice in November and SLP in December for ERA-Interim. (b) (black)

MCAcat_SCE, (red) MCAcat_SIC and (green) atmospheric SLP yearly time series from the

MCA (normalized).

Figure 14 :

Regression slopes of a bivariate regression of the SLP (in hPa) for the (a) MCA-snow, and

(b) MCA-SIC indices. Colors indicate level of significance below 10%.

Figure 15 :

Regression slopes of a multivariate regression of the SLP (in hPa) onto the (a) snow

dipole, (b) Barents-Kara Sea SIC and (c) SCA indices. In (a-c) colors indicate level of

significance below 10%. (d) R^2 value of univariate regressions using the AO index as

predictand and snow dipole, Barents-Kara Sea SIC or SCA as predictor. ALL indicates the

R^2 when using the three indices in a multivariate regression. Note that the y-axis is

different for observation (bars, left axis) and models (symbols, right axis).

The black symbols (bars) provide the results for models (observations), thick symbols

(bars) indicating level of significance of R^2 below 10%.

Figure A1 :

(a) Homogeneous October snow cover fraction (in %) and November heterogeneous SLP

(in hPa) covariance maps for the first MCA mode, when the snow cover leads by one

44

1014   month the atmosphere, for ERA-Interim during 1979-2014. (b) Same as (a) but for the

1015   1979-2005 period. (c) Same as (a) but using the December SLP. (d) Same as (c) but for

1016   the 1979-2005 period.
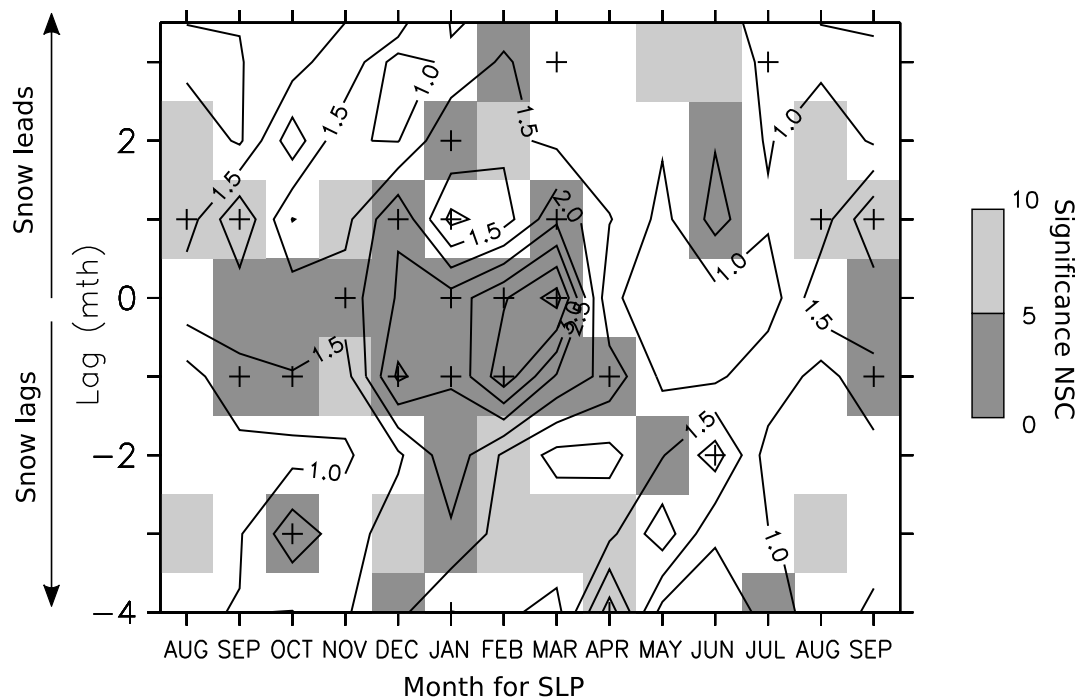
Fig. 1 : Normalized squared covariance (NSC, contours, in %) for the first MCA mode between observed SLP and Eurasia snow cover, for each month in the atmosphere. The lag is positive when the snow cover leads SLP. The gray shade provides the level of statistical significance for NSC. The plus symbols indicate the atmospheric month and time lag where the level of significance for the correlation (R) is below 5%.
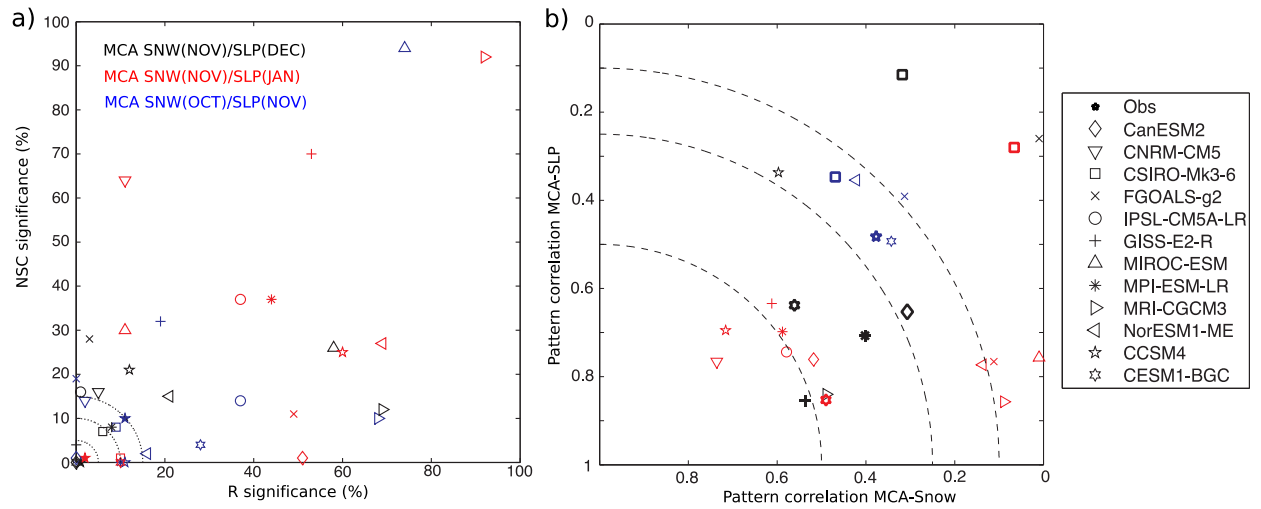
Fig. 2 : (a) Scatter plot of the confidence level, in %, of the normalized squared covariance, NSC, versus that of the correlation, R, for the first MCA mode between SLP and Eurasian snow cover. (b) Scatter plot of the spatial correlation between the SLP covariance map found in models and that of ERA-Interim, versus the spatial correlation between the snow cover covariance map found in models and that of ERA-Interim. The black indicates the results for SLP in December and SCE in November (one month lag). The blue indicates the results for SLP in November and SCE in October (one month lag). The red indicates the results for the SLP in January and SCE in November (two month lag). In (b), the bold symbols indicate levels of significance lower than 15% for both NSC and R.
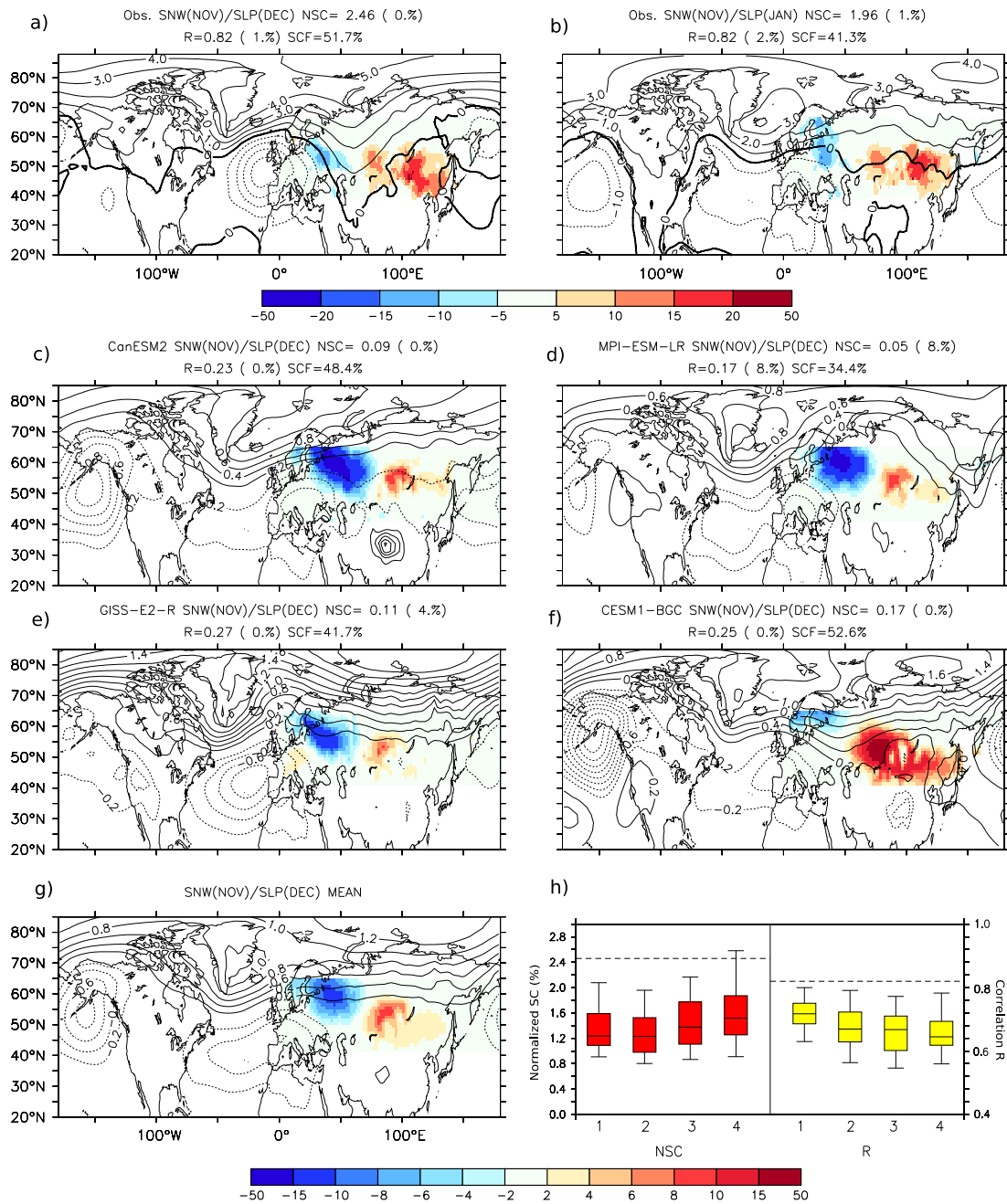
Fig. 3 : (a) Homogeneous snow cover fraction (in %) and heterogeneous SLP (in hPa) covariance maps for the first MCA mode, for December SLP and November snow cover, when the snow cover leads by one month the atmosphere, in ERA-Interim. (b) Same as (a), but using January SLP with a 2 month lag. (c), (d), (e), (f) and (g) same as (a) but for CanESM2, MPI-ESM, GISS-E2-R, CESM1-BGC and the mean of the four models,

respectively. Note that the color scale is different for observation and models. (h) Box plots of the NSC and R statistics from the MCA using 36-yr periods extracted from the control runs of each models (1: CanESM2, 2:MPI-ESM, 3: GISS-E2-T and 4: CESM1-BGC), error bars show the 5% and 95% percentiles. The dashed horizontal lines show the NSC and R values in observations.
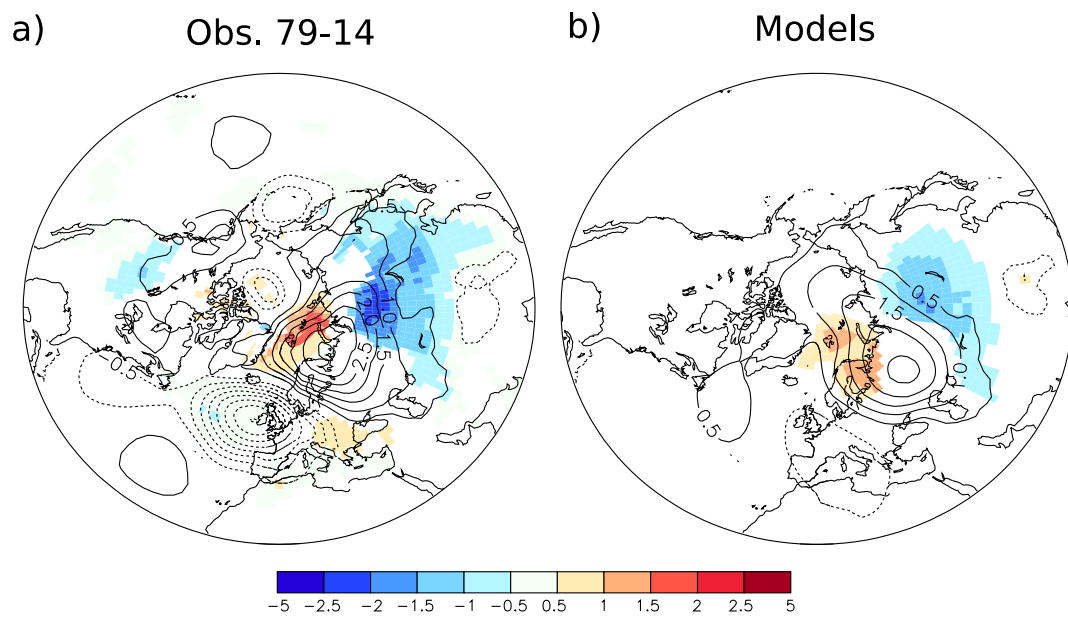
Fig. 4 : Regression of SLP (contours, in hPa) and 2m air temperature, (color, in K) on the MCA-snow index, in November, for (a) ERA-Interim and (b) the subset of four models. In (a), colors are masked if the level of significance is above 10% for observation. In (b), colors indicate anomalies of the same sign among the four models.
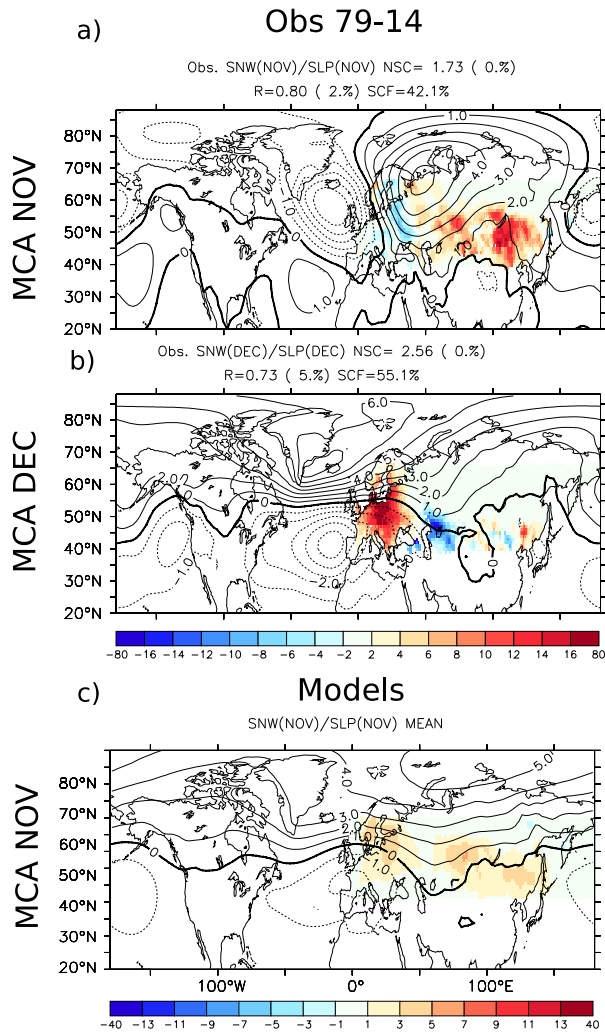
Fig. 5 : Homogeneous SLP (in hPa) and heterogeneous snow cover (in %) covariance maps for the first MCA mode, when the SLP and snow cover are simultaneous (no lag), for (a) November fields in ERA-Interim; (b) December fields in ERA-Interim and (c) November fields in the mean of the four models subset.
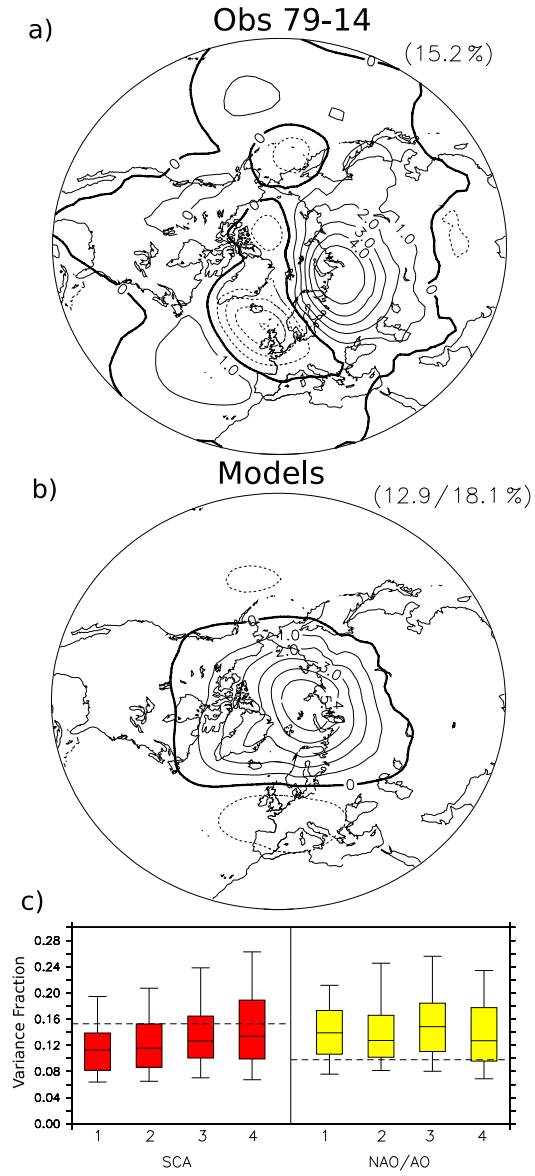
Fig. 6 : (a) REOF1 of November SLP (in hPa) in ERA-Interim. (b) Same as (a) for the model mean REOF1 using the four models. In (a), the variance fraction is given in parenthesis. In (b), the minimum and maximum variance fraction among the four models is indicated in parenthesis. (c) Box plots of the November variance (in %) explained by the SCA and the NAO/AO in 36-yr chunks from the control runs of each models (1: CanESM2, 2:MPI-ESM, 3: GISS-E2-R and 4: CESM1-BGC); the error bars give the 5% and 95% percentiles, and the dashed horizontal lines the AO and SCA variance fraction in observations.
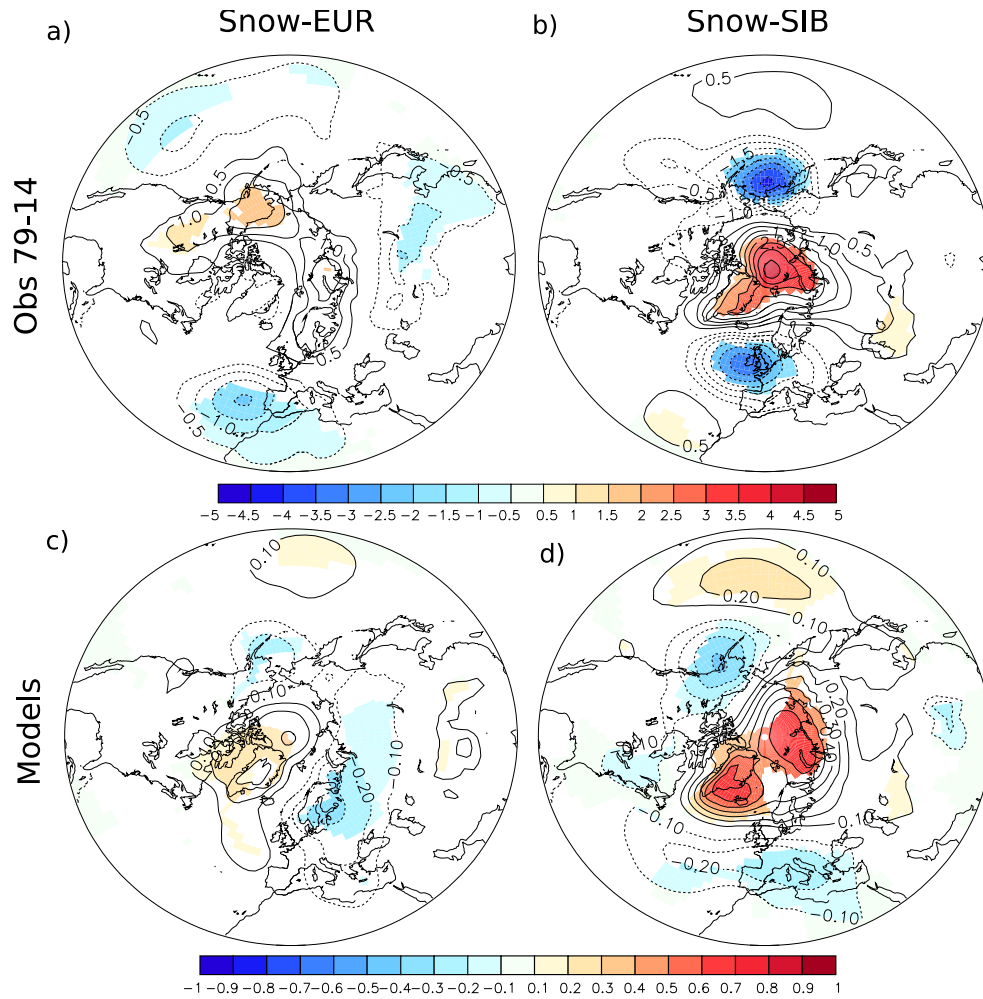
Fig. 7: Regression of the December SLP in hPa onto (Left) European and (Right) Siberian snow anomalies, given by multivariate regression; for (upper) ERA-Interim and (lower) the subset of four models. In (a) and (b), colors are masked if the level of statistical significance is above 10%. In (c) and (d), colors indicate anomalies of the same sign among the four models.
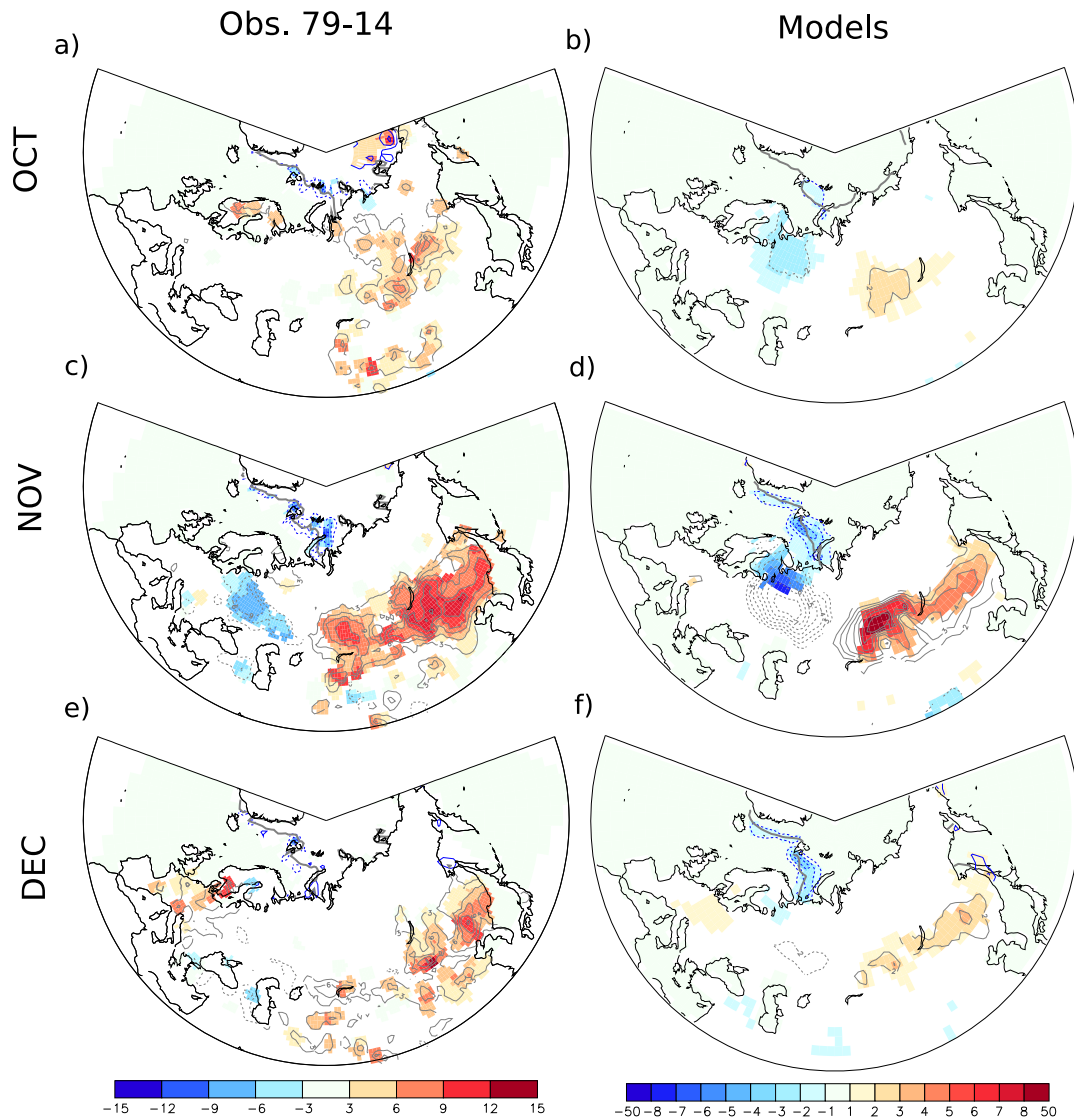
Fig. 8 : Regression of the snow cover fraction (color shades over continent, in %) and sea ice concentration (blue contours and shades over the ocean, in %), onto the November MCA-snow index, for (a) ERA-Interim in October; (b) the four models in October; (c) and (d) Same as (a) and (b) for November; (e) and (f) same as (a) and (b) for December. The sea-ice concentration contour interval is 5% in observations, and 1% for models, the zero contour is removed. The thick gray contour provides the 50% contour for climatological SIC.
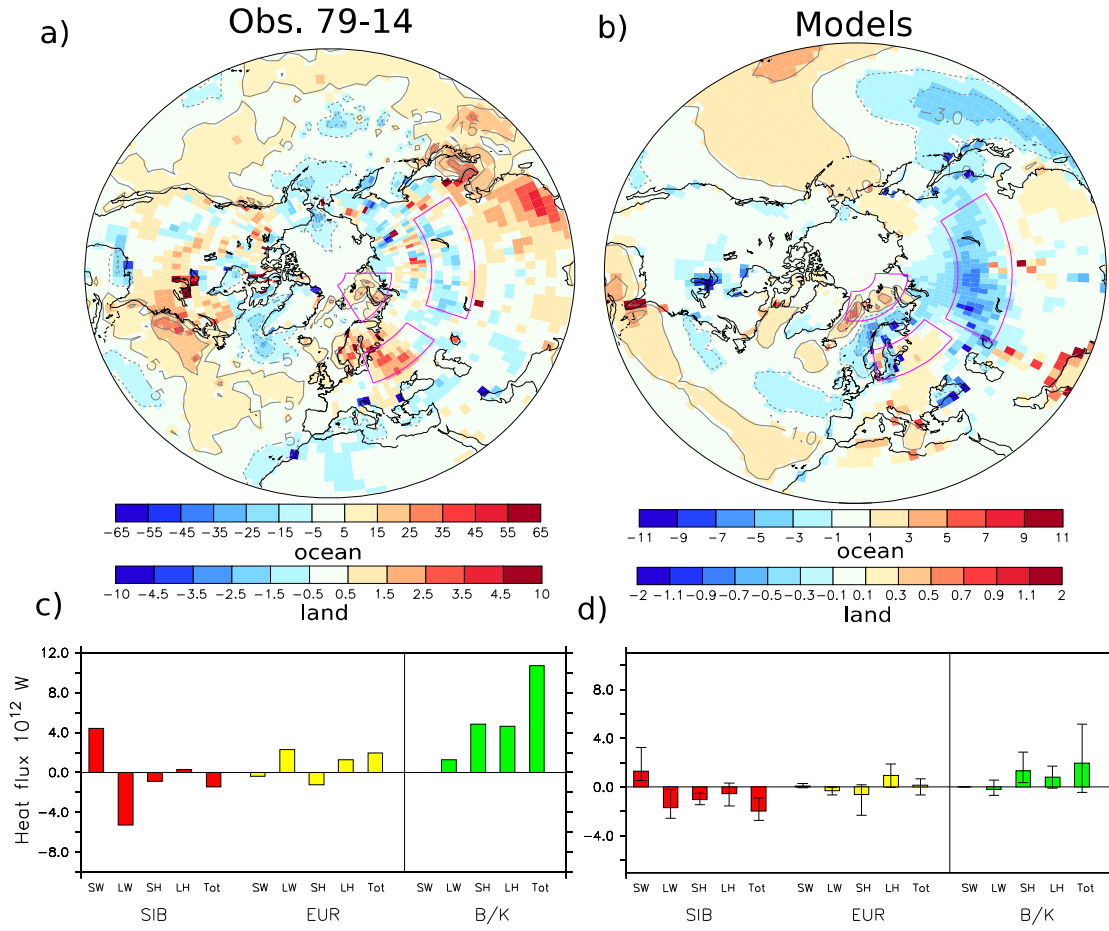
Fig. 9 : Thermodynamical component of the heat flux, positive upward, in W m^{-2}, associated in November with the November MCA-snow index in (a) ERA-Interim and (b) the four models. The color scale is different over land and ocean to emphasize the changes over continental surfaces. Note the different contour intervals for ERA-Interim and models. (c,d) Regressions of the shortwave (SW), longwave (LW), sensible (SH), latent (LH) and total (Tot) heat flux over the Siberia (SIB), Europe (EUR) and Barents-Kara Sea (B/K) integrated over boxes shown in (a) and (b) with histograms for (c) ERA-Interim and (d) the four models mean. In (d) the error bars indicate the minimum and maximum values among models.
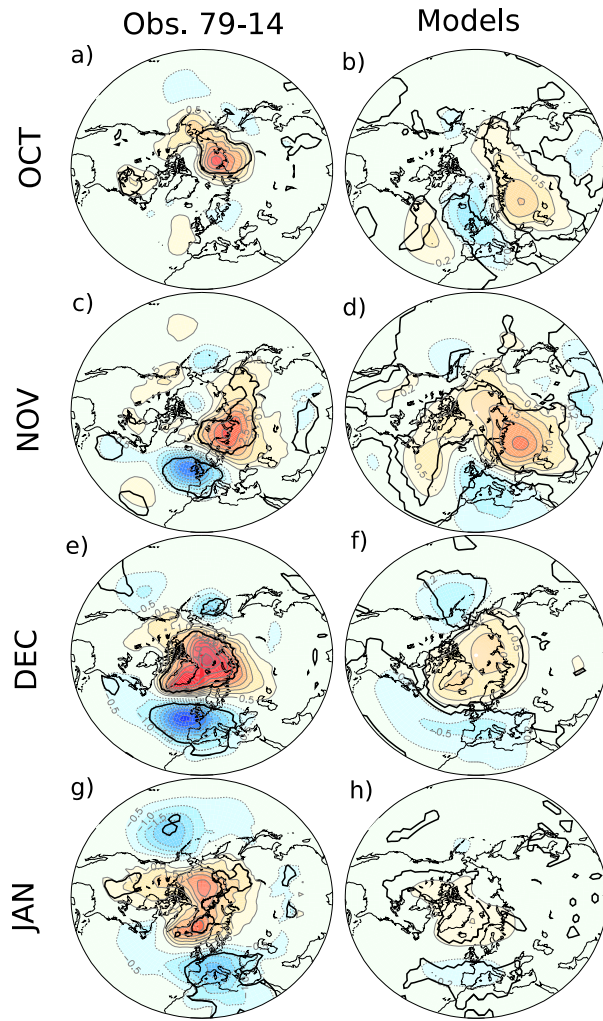
Fig. 10 : Regression of the SLP, in hPa (contour interval 0.5 hPa), onto the MCA-snow index, (left column) ERA-Interim and (right column) models, in (a), (b) October; (c), (d) November; (e), (f) December and (g), (h) January . The thick black line indicates 5% significance for observations or anomalies of the same sign among the four models. The contour interval at -0.2 and 0.2 hPa was added for models.
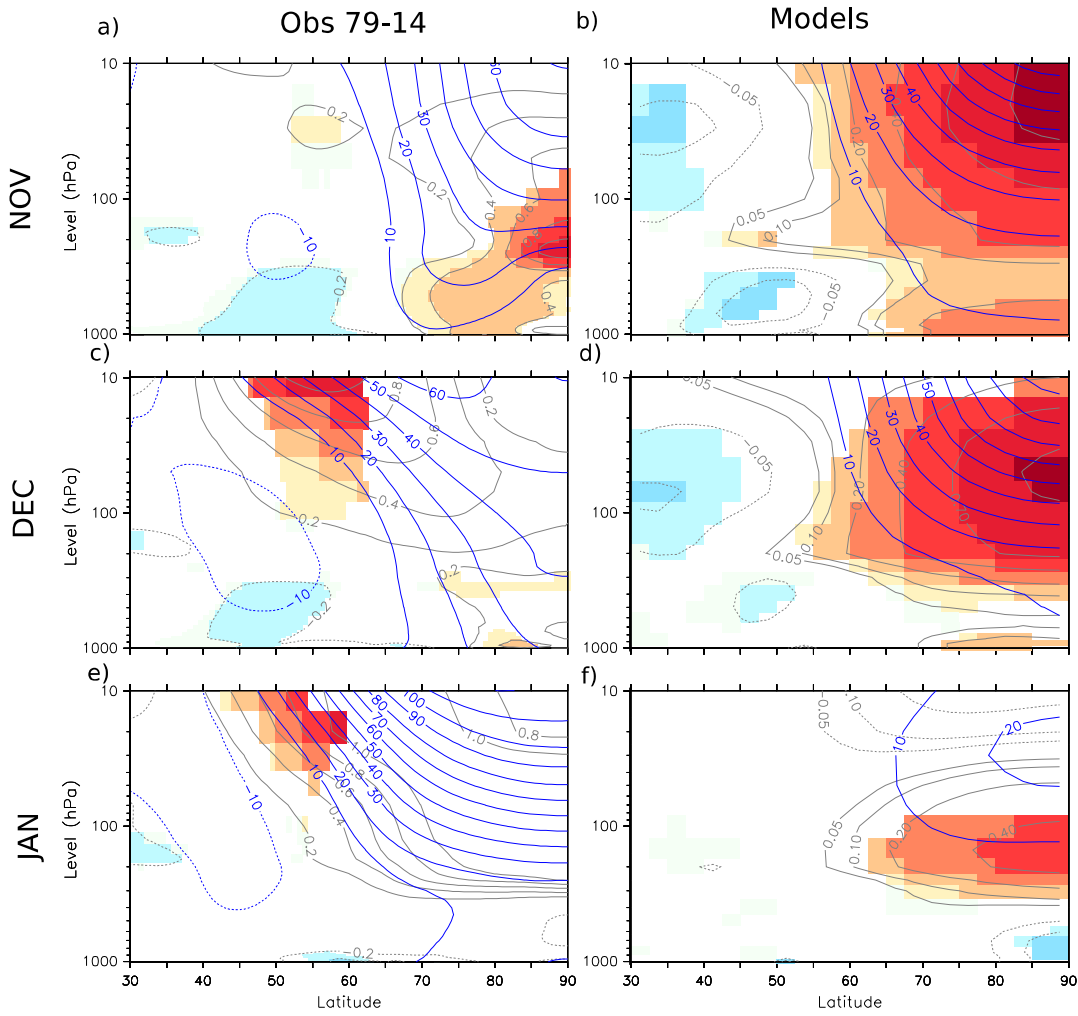
Fig. 11 : Regression of the zonal-mean temperature (gray contours and color shades, in K) and geopotential height (blue contours, in m) onto the MCA-snow normalized index, for (left column) ERA-Interim and (right column) models, in (a), (b) November; (c), (d) December and (e), (f) January. Colors indicate zonal mean temperature (left) level of significance below 10% or (right) anomalies of the same sign among the four models.
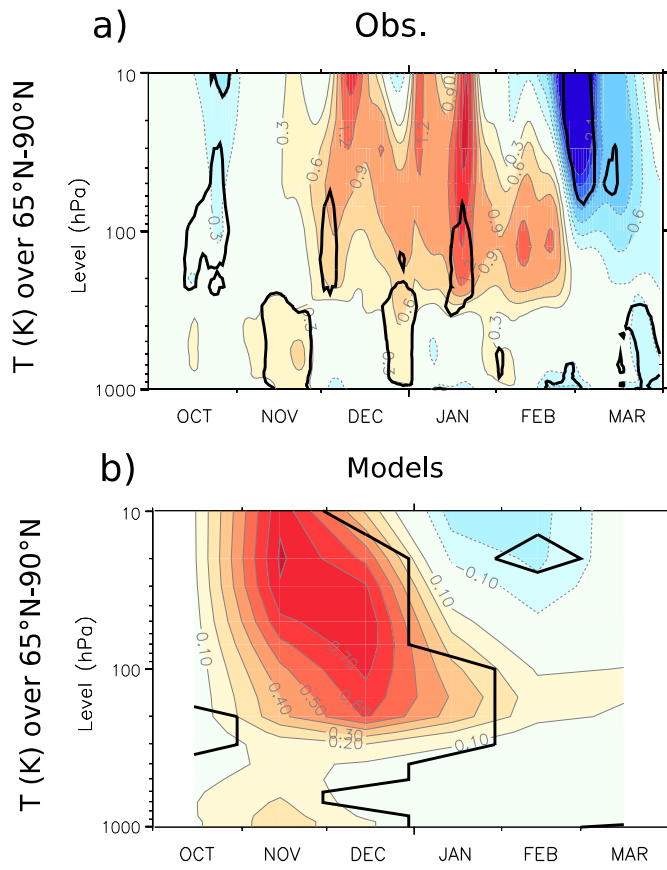
Fig. 12 : Regression of the temperature over the polar cap (65°N-90°N) onto the MCA-snow normalized index, for (a) ERA-Interim and (b) models. The thick black lines indicate (a) level of significance below 10% or (b) anomalies of the same sign among the four models. Note the different contour intervals.
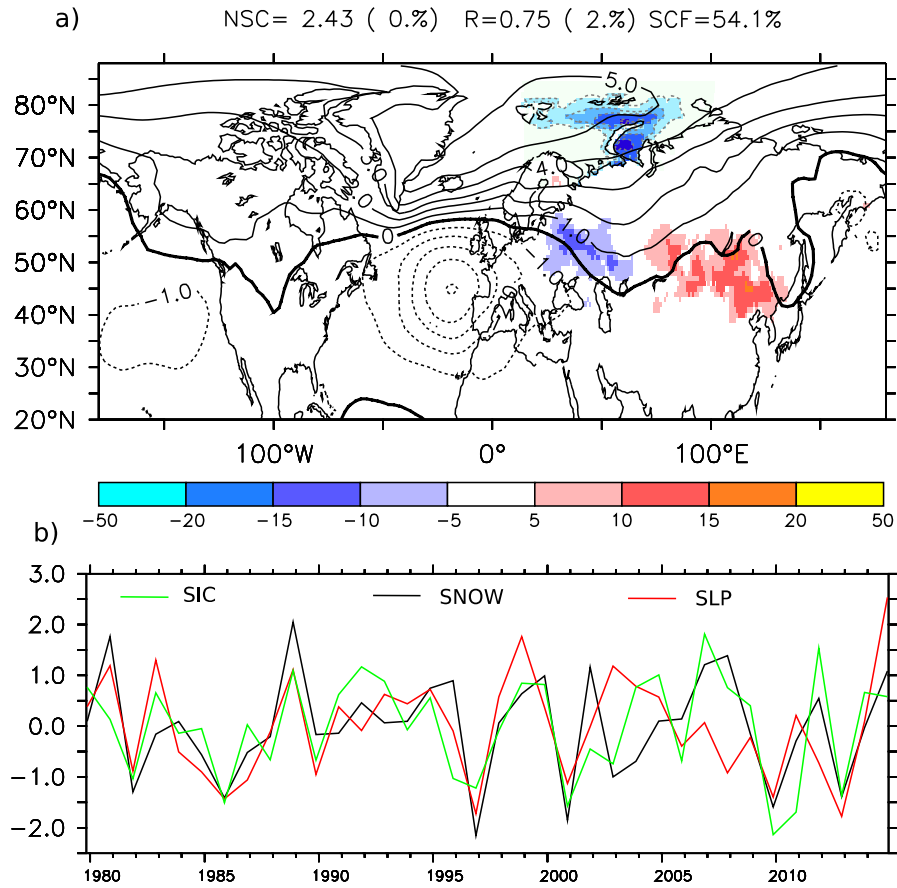
Fig. 13 : (a) Snow cover (color over land, in %) and SIC (color over ocean, in %) homogeneous covariance map and SLP (in hPa) heterogeneous map for the first MCA mode using combined snow/sea-ice in November and SLP in December for ERA-Interim. (b) (black) MCAcat_SCE, (red) MCAcat_SIC and (green) atmospheric SLP yearly time series from the MCA (normalized).
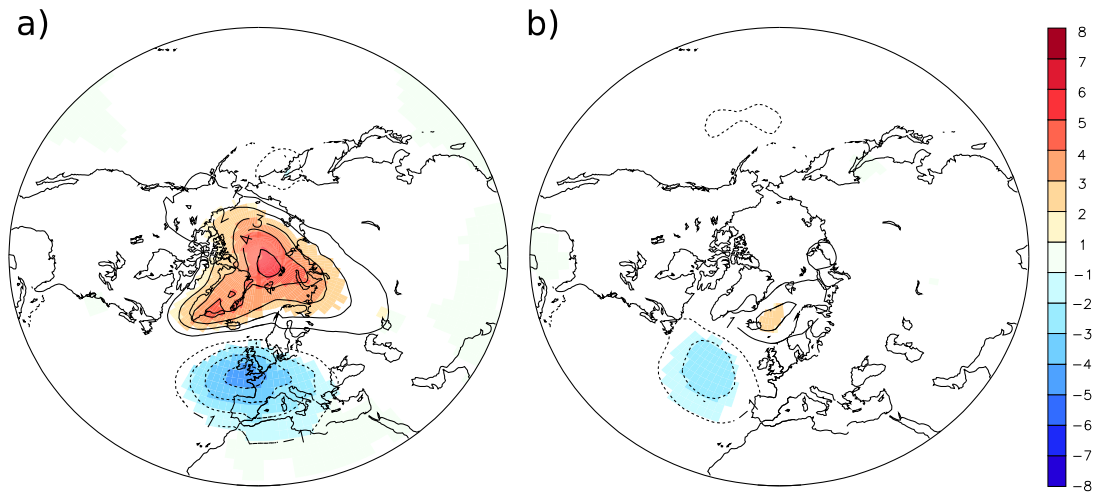
Fig. 14: Regression slopes of a bivariate regression of the SLP (in hPa) for the (a) MCA-snow, and (b) MCA-SIC indices. Colors indicate level of significance below 10%.
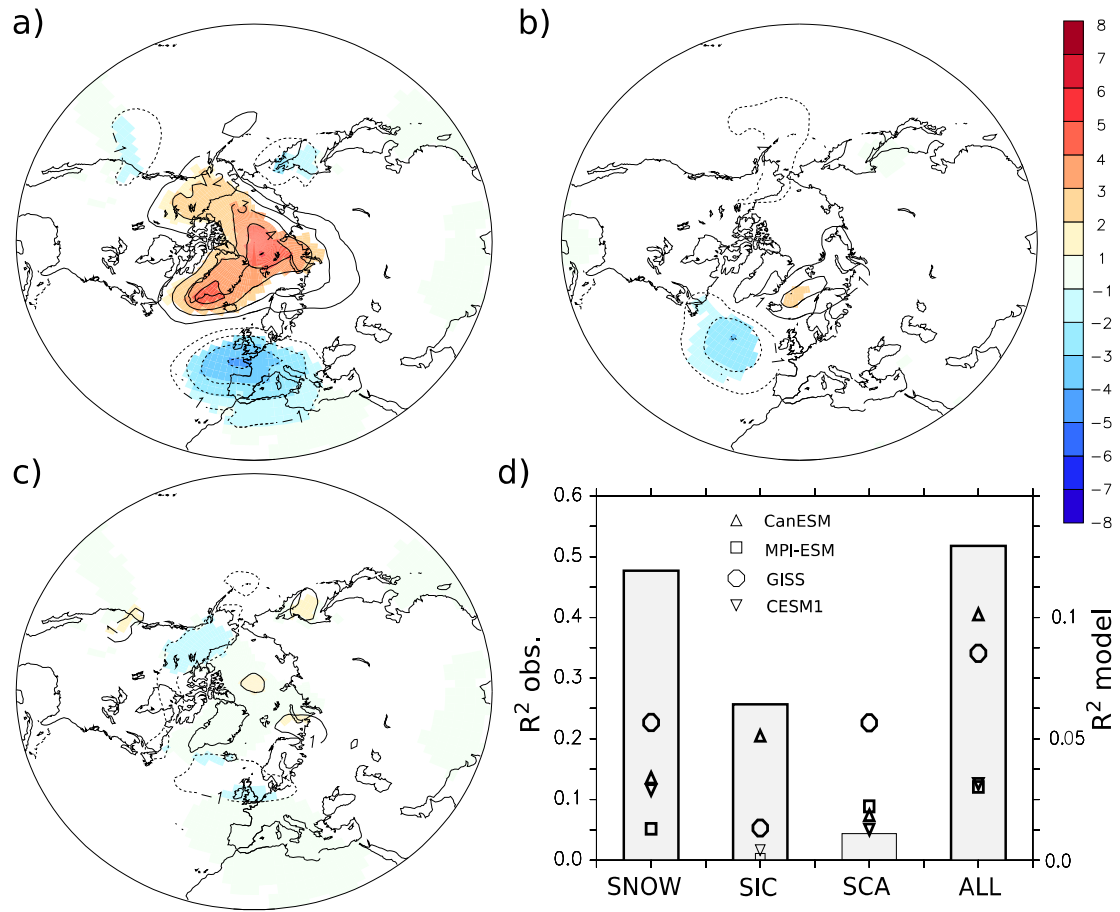
Fig. 15 : Regression slopes of a multivariate regression of the SLP (in hPa) onto the (a) snow dipole, (b) Barents-Kara Sea SIC and (c) SCA indices. In (a-c) colors indicate level of significance below 10%. (d) R^2 value of univariate regressions using the AO index as predictand and snow dipole, Barents-Kara Sea SIC or SCA as predictor. ALL indicates the R^2 when using the three indices in a multivariate regression. Note that the y-axis is different for observation (bars, left axis) and models (symbols, right axis).

The black symbols (bars) provide the results for models (observations), thick symbols (bars) indicating level of significance of R^2 below 10%.
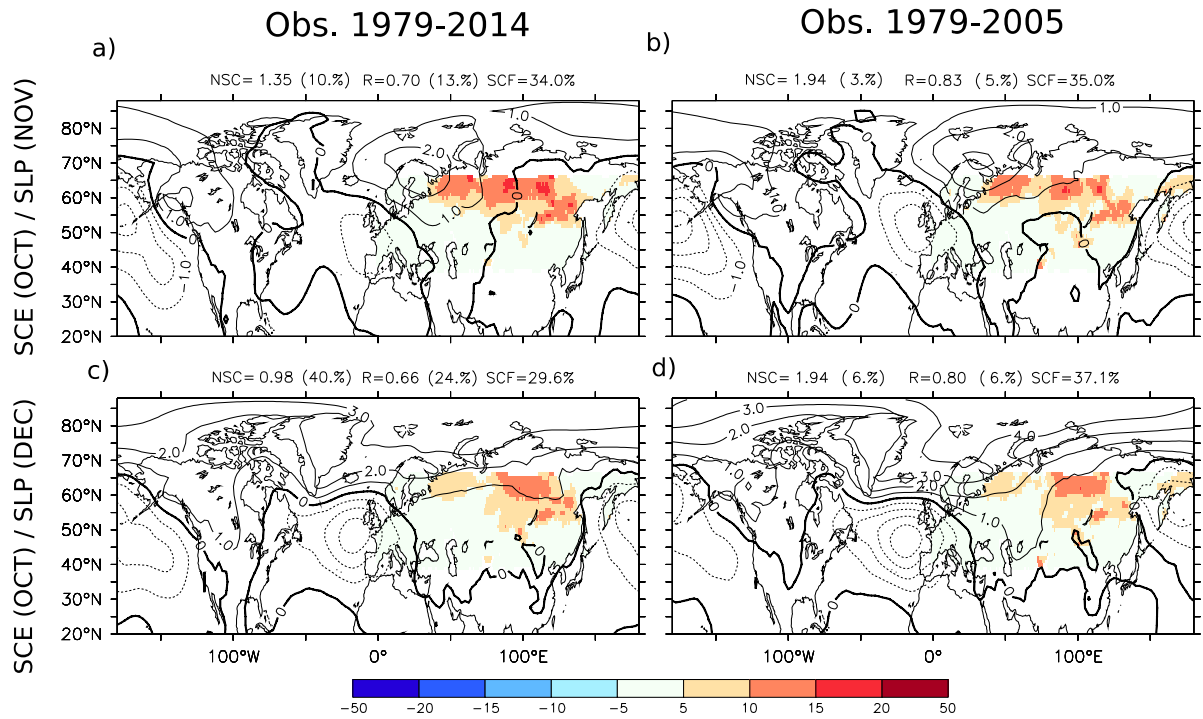
Fig. A1 : (a) Homogeneous October snow cover fraction (in %) and November heterogeneous SLP (in hPa) covariance maps for the first MCA mode, when the snow cover leads by one month the atmosphere, for ERA-Interim during 1979-2014. (b) Same as (a) but for the 1979-2005 period. (c) Same as (a) but using the December SLP. (d) Same as (c) but for the 1979-2005 period.